Waning of immunity by pathogen evolution

PhD Thesis

Golsa Sayyar

Supervisors:

Dr. Gergely Röst

Dr. Ábel Garab

Doctoral School of Mathematics
University of Szeged, Bolyai Institute

Acknowledgments

I would like to express my gratitude to Dr. Gergely Röst for his guidance during the writing of both papers.

I am especially grateful to Dr. Ábel Garab for his invaluable help, his patience in answering my questions, and his prompt, thorough responses. His support was essential in completing my second paper and improving my thesis.

I also extend my sincere thanks to Professor Kieran Sharkey for kindly hosting me at the University of Liverpool for over eleven months and for always being available to support my research whenever I needed assistance.

I also gratefully acknowledge the financial support provided by the Marie Curie Grant, which allowed me to fully dedicate myself to my work.

Last but not least, I want to thank my beloved family for their constant love and support throughout this journey.

Contents

List of Figures

List of Tables

1 Forewords

The aim of this research is twofold: first, it involves developing deterministic and stochastic models to simulate the spread of infectious diseases. Second, inspired by COVID-19, we aim to explore how immunity, shaped by pathogen evolution, influences the dynamics of outbreaks.

In Chapter 1, we begin with an overview of the fundamental SIR epidemiological model, followed by a detailed discussion of its key features, such as equilibrium points and stability, which are essential for analyzing the model's behavior. The chapter also addresses the evolutionary dynamics of infectious diseases, with a particular focus on viral evolution in the context of COVID-19.

In Chapter 2, we propose two epidemiological models of disease transmission dynamics that accounts for the emergence of new strains through virus mutations, inspired by the COVID-19 pandemic. We analyze how time varying social distancing measures and differing assumptions about cross-immunity affect disease prevalence and strain dynamics. Our findings highlight that while a sequential pattern of strain replacement occurs when immunity is only against earlier strains, more complex dynamics, such as the co-circulation of multiple strains, emerge when immunity is strain-specific. These results are compared with genomic patterns observed during the COVID-19 pandemic.

Chapter 3 of this thesis explores the application of the SIR model within network structures. The chapter emphasizes the need for stochastic modeling to capture the complexities of disease transmission, particularly in the context of COVID-19. By analyzing the dynamics of virus spread across different network, it investigates how network features influence disease propagation. The chapter also examines the effects of viral mutations and immunity on transmission patterns and evaluates the efficacy of global social distancing strategies in controlling outbreaks.

Chapter 4 addresses the challenge of predicting viral evolution by developing a novel model by considering a trade-off between immunity evasion and transmissibility. The model identifies that highly transmissible strains tend to evolve toward immune evasion, while less contagious strains shift toward increased transmissibility. By assuming a linear trade-off, we derive a non-linear difference equation to describe long-term evolutionary patterns. Our analysis provides criteria for evolutionary convergence, identifies cyclical patterns in strain evolution, and reveals conditions under which viral evolution becomes chaotic. Visualization through bifurcation diagrams highlights complex dynamic behaviors, offering new insights into the interplay between immune evasion and transmissibility in viral evolution.

2 Introduction

Infectious diseases have been intertwined with the story of humanity from the very beginning, leaving lasting marks on human civilization. The Athens plague of 430 BC and the 14^{th}-century Black Death—which wiped out nearly one-third of Europe's population—are prime examples of how these diseases have critically influenced human history. The 1918 influenza pandemic, also known as the Spanish flu, is an example of such devastating effects, with an estimated 50 million fatalities globally [51, 81]. In the modern era, notable events include the emergence of HIV/AIDS, the Ebola outbreaks in West Africa, and the COVID-19 pandemic, with the latter having significantly reshaped the world since it began.

However, the mathematical analysis of infectious diseases and their spread is relatively recent, spanning approximately 350 years. The process of mathematical modeling begins with a clear description of infectious diseases, followed by the identification of key factors that influence real-life behavior. This process involves simplification and logical analysis, which are essential for creating useful models. Mathematical modeling offers a powerful tool for analyzing the complexities of infectious diseases, allowing researchers to gain insights into their dynamics and develop strategies for control and prevention [51].

Significant advancements in the mathematical modeling of infectious diseases were made in the early twentieth century. William Hamer's work on explaining the recurrence of measles marked a notable milestone in this field [18]. Since then, mathematical models have become essential tools in epidemiological research, offering frameworks to understand disease spread. One of the most widely used approaches is compartmental modeling, where the population is divided into different groups based on their disease status. These models are particularly useful for providing simplified insights into the dynamics of infectious diseases. For example, the SIR (Susceptible, Infectious, Removed) model divides individuals into three distinct categories to track the progression of an outbreak in a population [35, 42].

However, not all models fit neatly into the compartmental framework. More complex models, such as agent-based models (ABMs), simulate the behavior of individuals or agents within a population to capture the stochastic and spatial aspects of disease transmission [26, 76]. ABMs offer a more granular approach, representing interactions at an individual level and allowing for heterogeneity in behaviors and outcomes.

Within the broader class of compartmental models, the SIR model serves as a foundational example, offering a clear structure to study the transmission dynamics

of infectious diseases. This model simplifies real-world complexities but has proven invaluable in understanding the basic mechanisms of disease spread and control strategies.

Within the SIR model framework:

- Susceptible individuals are those not yet immune to the disease, placing them at risk of infection upon exposure.
- Infectious individuals are actively carrying the disease and are capable of spreading it to susceptible contacts.
- Removed individuals have acquired immunity, either through recovery or vaccination, and therefore no longer contribute to the transmission of the disease.

This structured approach has profoundly influenced our understanding of how diseases spread and the effectiveness of interventions to control outbreaks.

The number of individuals in each of these classes changes with time, that is, $S(t)$, $I(t)$, and $R(t)$ are functions of time t. The total population size N is the sum of the sizes of these three classes and remains constant over time, i.e.,

$$N = S(t) + I(t) + R(t),$$

where N can be assumed to be normalized to $N = 1$.

A simple SIR model with incorporation of demographic term is given by the following system of ODEs where each differential equation shows how the classes change over time [18]. The generation of susceptible individuals in this model is given by recruitment rate $\mu > 0$, which is also equal to the per capita death rate. Upon infection, these susceptible individuals move to the infected compartment I at a rate denoted by $\beta S(t)I(t)$. Here, parameter β signifies the transmission rate of the disease. Subsequently, the infected individuals undergo recovery at a rate $\gamma I(t)$, where $\gamma > 0$ is the disease recovery rate, leading them to transition to the class R:

$$\begin{aligned} \dot{S}(t) &= -\beta S(t)I(t) + \mu - \mu S(t), \\ \dot{I}(t) &= \beta S(t)I(t) - \gamma I(t) - \mu I(t), \\ \dot{R}(t) &= \gamma I(t) - \mu R(t). \end{aligned} \tag{2.1}$$

One essential tool in understanding the dynamics of infectious diseases is the basic reproduction number which indicates whether a disease will persist in a population or diminish over time. This value represents the average number of secondary cases generated by a single infectious individual in a population where everyone is susceptible.

Given the assumption that initially the whole population is susceptible, the basic reproduction number, denoted as $\mathcal{R}_0$, measures the ability of the pathogens to invade the susceptible population. When $\mathcal{R}_0 < 1$, it leads to a gradual decline in the number of infected individuals, eventually resulting in the disease's eradication from the

population. Conversely, an $\mathcal{R}_0 > 1$ indicates the disease's capability to maintain its presence and become endemic within the population.

To interpret $\mathcal{R}_0$ of Model (2.1), we consider that the number of new cases per unit of time generated by all infectious individuals is given by βSI. When there is a few infectious individual (i.e., $I = \epsilon$), and the entire population consists of susceptible individuals (i.e., $S = N = 1$), then the number of secondary cases produced by one infectious individual in a unit of time is β. Considering that one infectious individual remains infectious for $\frac{1}{\gamma+\mu}$ time units, the total number of secondary cases that it will produce during its lifespan on average is $\mathcal{R}_0 = \frac{\beta}{\gamma+\mu}$.

Now, we can explore some properties of the system. This model has been exceptionally valuable, especially for (1) determining disease prevalence at equilibrium and (2) identifying the conditions required for the stability of endemic equilibrium.

2.1 The Equilibrium Points of the SIR Model with Demography

Incorporating host demographic dynamics into models enables a disease to sustain itself within a population over an extended period.

Equilibrium points are crucial for understanding the long-term behavior of dynamical systems, including the analysis of biological models. They help predict the conditions under which a system can maintain stability or experience change, providing insights into system behavior under various initial conditions and perturbations. To explore when the system is at equilibrium, we equate each equation to zero and solve for the equilibrium values of the variables. The disease-free equilibrium, which emerges trivially, refers to a state in the model where the entire population is susceptible to the disease, and there are no infected or infectious individuals present. This equilibrium is mathematically denoted as $(S^*, I^*, R^*) = (1, 0, 0)$.

To determine the endemic equilibrium, where the disease persists within the population, we begin by setting the infection rate equation to zero:

$$\dot{I}(t) = \beta S(t)I(t) - \gamma I(t) - \mu I(t) = 0.$$

By factoring I, we have

$$I(t)(\beta S(t) - \gamma - \mu) = 0,$$

which leads to either $I^* = 0$ or $S^* = \frac{\gamma+\mu}{\beta} = \frac{1}{\mathcal{R}_0}$. $I^* = 0$ implies the disease-free equilibrium, so we focus on the second condition and substitute it into the first equation of Model (2.1) for I^*. After some calculation, we finally have:

$$I^* = \frac{\mu}{\beta}(\mathcal{R}_0 - 1).$$

Having $S^* + I^* + R^* = 1$, we can easily obtain $R^* = \frac{\gamma}{\beta}(\mathcal{R}_0 - 1)$. The endemic equilib-

rium can, therefore, be described by:

$$(S^*, I^*, R^*) = \left(\frac{1}{\mathcal{R}_0}, \frac{\mu}{\beta}(\mathcal{R}_0 - 1), \frac{\gamma}{\beta}(\mathcal{R}_0 - 1) \right), \tag{2.2}$$

Note that the condition $\mathcal{R}_0 > 1$ necessitates the relation $\beta > \gamma + \mu$. This assumption ensures that the endemic steady state exists and is biologically meaningful.

2.1.1 Stability Analysis for the SIR Model with Demography

Now, we will provide conditions on the parameter values that are necessary for the equilibrium to be (asymptotically) stable to small perturbations.

Definition 2.1.1 (Lyapunov Stability)**.** *Consider an ordinary differential equation*

$$\dot{x} = f(x), \quad x \in \mathbb{R}^n. \tag{2.3}$$

Let x^* be an equilibrium point, i.e., $f(x^*) = 0$. The equilibrium x^* is said to be (Lyapunov) stable if for every $\epsilon > 0$, there exists a $\delta > 0$ such that if $\|x(0) - x^*\| < \delta$, then for all $t \geq 0$,

$$\|x(t) - x^*\| < \epsilon. \tag{2.4}$$

This means that trajectories starting sufficiently close to x^* remain close for all time.

If, in addition, there exists $\delta' > 0$ such that $\|x(0) - x^*\| < \delta'$ implies

$$\lim_{t \to \infty} x(t) = x^*, \tag{2.5}$$

then x^* is called asymptotically stable.

If x^* is not stable, it is called unstable.

Thus, if the equilibrium is asymptotically stable, small perturbations or deviations from this point will decay over time, leading the system back to its equilibrium state. Conversely, if the equilibrium is unstable, these deviations will grow over time, causing the system to diverge from the equilibrium [39].

To find the stability of equilibrium points corresponding to Model (2.1), we determine the eigenvalues of the Jacobian matrix at the equilibrium. Stability is guaranteed if the real part of all eigenvalues are negative. The matrix at equilibrium is given by:

$$J = \begin{pmatrix} -\beta I^* - \mu & -\beta S^* & 0 \\ -\beta I^* & \beta S^* - (\mu + \gamma) & 0 \\ 0 & \gamma & -\mu \end{pmatrix}.$$

The eigenvalues of this matrix, λ_i, for $i = 1, 2, 3$, are the solutions of $\det(J - \lambda I) = 0$; where I is the identity matrix. This gives:

$$\left[(\beta I^* - \mu - \lambda)(\beta S^* - \mu + \gamma + \lambda) + \beta^2 I^* S^* \right] (-\mu - \lambda) = 0.$$

Now, to obtain the three eigenvalues, we need to substitute both the disease-free equilibrium and the endemic equilibrium into S^*, I^*, and R^*.

Let us first consider the disease-free equilibrium. After few lines of algebra, we obtain the three eigenvalues $\lambda_{1,2} = -\mu$ and $\lambda_3 = \beta - (\mu + \gamma)$. To achieve stability in this equilibrium, it is imperative that all eigenvalues are negative. This requirement establishes the stability criterion as $\beta < (\mu + \gamma)$. In practical terms, this means that the condition for stability is ensuring that the basic reproduction number, $\mathcal{R}_0$, is less than 1.

To further investigate the endemic equilibrium, we substitute the expressions for S^* and I^* into equation (2.2). Our goal is to determine the conditions under which all the eigenvalues have negative real parts. After simplifications, we obtain the following eigenvalues:

$$\lambda_1 = -\mu,$$

$$\lambda_2 = -\frac{\mu\mathcal{R}_0}{2} + \frac{\sqrt{(\mu\mathcal{R}_0)^2 - 4\mu(\mathcal{R}_0 - 1)(\gamma + \mu)}}{2},$$

$$\lambda_3 = -\frac{\mu\mathcal{R}_0}{2} - \frac{\sqrt{(\mu\mathcal{R}_0)^2 - 4\mu(\mathcal{R}_0 - 1)(\gamma + \mu)}}{2}.$$

The first eigenvalue, $\lambda_1 = -\mu$, is always negative. The behavior of λ_2 and λ_3 depends on the expression under the square root, which is

$$\sqrt{(\mu\mathcal{R}_0)^2 - 4\mu(\mathcal{R}_0 - 1)(\gamma + \mu)}.$$

If this expression is positive, then λ_2 and λ_3 are real. In this case, $\lambda_{2,3}$ are clearly negative when $\mathcal{R}_0 > 1$, ensuring asymptotic stability. On the other hand, if the expression under the square root is negative, the square root term becomes imaginary, and the eigenvalues form a complex conjugate pair. The real part of both eigenvalues in this case is

$$\mathrm{Re}(\lambda_2) = \mathrm{Re}(\lambda_3) = -\frac{\mu\mathcal{R}_0}{2}.$$

Since $\mu\mathcal{R}_0$ is always positive, the real part of the complex eigenvalues remains negative, implying that the endemic equilibrium is asymptotically stable. Thus, for $\mathcal{R}_0 > 1$, all eigenvalues have negative real parts, confirming that the endemic equilibrium is asymptotically stable. This implies that the disease persists in the population at a stable endemic level.

2.2 Evolutionary Dynamics

Viral evolution is the process by which virus populations change over time due to mutations, recombination, and reassortment, and can lead to the emergence of new infectious diseases or change the epidemiology of existing ones. Antigenic drift and

shift in influenza viruses are prime examples of how viral evolution can affect disease patterns, leading to seasonal epidemics and occasional pandemics [41, 64].

Emerging infectious diseases often arise from zoonotic transmissions, where viruses evolve the ability to infect new host species, including humans. The spillover of SARS-CoV, MERS-CoV, and SARS-CoV-2 from animal hosts to humans exemplifies the critical role of viral evolution in infectious disease emergence. Mathematical modeling in viral evolution helps in quantifying these changes and predicting their impact on disease dynamics. Models can range from simple equations representing the basic reproduction number ($\mathcal{R}_0$) to complex simulations that account for genetic diversity within viral populations [11, 84].

In this section, our goal is to explore the evolution of parasites (including viruses) through the examination of the epidemiological dynamics when at least two parasite strains compete for the same host.

Consider the following equation where the two strains differ in their infectivity, β_1, and β_2, and in their degree of virulence, $\bar{v}_1$, and $\bar{v}_2$.

$$\begin{aligned} \dot{S}(t) &= \Lambda - S(t)(\beta_1 I_1(t) + \beta_2 I_2(t)) - \mu S(t), \\ \dot{I}_1(t) &= \beta_1 S(t) I_1(t) - \mu I(t) - \bar{v}_1 I_1(t), \\ \dot{I}_2(t) &= \beta_2 S(t) I_2(t) - \mu I(t) - \bar{v}_2 I_2(t), \end{aligned} \tag{2.6}$$

with Λ specifying the constant birth rate and μ their natural death rate.

The basic reproduction number of the two strains are given by $\mathcal{R}_{0i} = \frac{\beta_i}{\mu+\bar{v}_i}\frac{\Lambda}{\mu}$, where $i = 1, 2$. If $\mathcal{R}_{02} > \mathcal{R}_{01}$, then all infected individuals will eventually be infected with strain 2, leading to the extinction of strain 1. Consequently, evolutionary processes will prefer mutations that exhibit a higher basic reproduction number. In the absence of any trade-off between infectivity and virulence, evolutionary dynamics are expected to enhance the transmission rate while diminishing virulence (Chapter 11 of [64]).

Most public health concerns related to infectious diseases surprisingly do not conform to the anticipated patterns. This inconsistency has led to extensive research efforts, focusing on the trade-offs between a pathogen's transmission rate and the duration of its infectious phase [2, 37, 44]. The concept of a transmission–virulence trade-off suggests that infections that produce a high number of pathogenic particles, and thus are easily transmitted, tend to be more harmful to the host, potentially leading to rapid death of the host as outlined in [10, 20]. Depending on the relationship between transmission rate β and virulence $\bar{v}$, there might be an evolutionarily stable level of virulence that maximizes the basic reproduction number $\mathcal{R}_0$. In some scenarios, evolution may favor either extremely high or low levels of virulence. The specifics of these dynamics depend on the relationship between β and $\bar{v}$. For example, a linear relationship implies that $\mathcal{R}_0$, or the potential for an infection to spread, increases with virulence. Thus, in such scenarios, natural selection tends to favor more virulent, and by extension, more infectious strains. When the transmission rate is described by the saturating function $\frac{a\bar{v}}{c+\bar{v}}$, dependent on virulence with constant parameters a and c, it follows that the basic reproduction number exhibits a one-

peaked relationship with virulence (Fig. 2.1). The peak, representing the maximum value of $\mathcal{R}_0$, occurs at an intermediate virulence level, specifically at $\bar{v}^{max} = \sqrt{c\mu}$. For a parasite population with virulence exceeding $\bar{v}^{max}$, evolutionary pressures tend to decrease virulence. Conversely, if the population's virulence is below this optimal level, virulence is likely to increase [64].

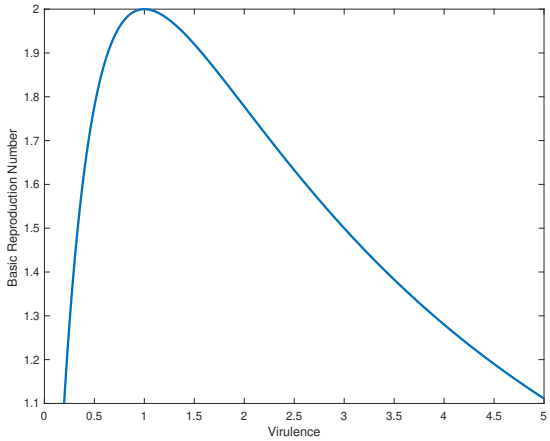

Figure 2.1: *The basic reproduction number distribution of strains with different range of virulence defined by the transmission rate–virulence trade-off:* $\beta = \frac{a\bar{v}}{c+\bar{v}}$. *With this trade-off, the basic reproduction number* $\mathcal{R}_0$ *for each strain of Model* (2.6) *is given by* $\mathcal{R}_{0i} = \frac{\Lambda a\bar{v}_i}{\mu(c+\bar{v}_i)(\mu+\bar{v}_i)}$, *when* $\Lambda = 1$, $a = 8$, *and* $c = \mu = 1$. *Hence, within the competitive dynamics of these two strains, evolution favors the strain whose virulence is nearest to* 1, *as it exhibits the greatest* $\mathcal{R}_0$.

In Chapter 5, we present a novel model of viral evolution that incorporates the trade-off between immune evasion and transmissibility. Our analysis begins with the baseline Model (2.1), which considers a single resident strain in isolation. New strains emerge as mutations when the system is at endemic equilibrium (2.2). This chapter explores the long-term evolutionary dynamics of these emergent viral strains and examines the intricate relationship between transmissibility and immune evasion, highlighting the impact of this trade-off on viral persistence and adaptation.

2.3 COVID-19

The COVID-19 pandemic, caused by the severe acute respiratory syndrome coronavirus 2 (SARS-CoV-2), has proved to be exceptionally contagious, sparking a global health crisis unparalleled since the 1918 flu pandemic [23]. The pandemic has, as of March 2024, led to over 750 million cases and more than 20 million deaths, as reported by the World Health Organization's (WHO) COVID-19 dashboard [83].

Since its onset, the pandemic has been compounded by the emergence of multiple variants of concern (VOC). These variants, including Alpha, Beta, Gamma, Delta,

and Omicron, have presented distinct challenges in disease transmission and vaccine efficacy [31, 32].

The Alpha variant (B.1.1.7), first detected in the United Kingdom, exhibited increased transmissibility and the potential to evade immune defenses. Similarly, the Beta variant (B.1.351), originating in South Africa, raised concerns about reduced vaccine efficacy and the risk of reinfection. The Gamma variant (P.1), identified in Brazil, showed heightened transmissibility and an increased risk of severe outcomes. The Delta variant (B.1.617.2), originating in India, demonstrated even greater transmissibility and partial immune evasion, necessitating enhanced public health measures. Most recently, the Omicron variant (B.1.1.529), discovered in South Africa, has presented as the most infectious variant yet, with significant mutations in the spike protein [7, 69].

In the midst of the global spread of these variants, mathematical models have played a crucial role in informing public health responses. Classical SIR models, commonly used during epidemics [5, 25], have been adapted to incorporate nuances specific to COVID-19, including asymptomatic and symptomatic infections, hospitalizations, and quarantine measures [38, 71]. These models have been instrumental in evaluating the effectiveness of non-pharmaceutical interventions (NPIs) implemented by governments worldwide.

Social distancing stands out as a key strategy among NPIs for combatting the spread of COVID-19. Despite its efficacy in reducing transmission rates, social distancing measures have sparked apprehensions regarding their economic repercussions. However, rigorous mathematical modeling has illuminated the comparative economic benefits of social distancing over other measures like quarantine or isolation. By quantifying the economic costs and benefits associated with various intervention strategies, these models assist policymakers in crafting nuanced approaches that strike a balance between public health protection and economic stability [66].

In Chapter 3, we introduce two different scenarios for COVID-19 that include emergence of new strains due to mutations. We then explore how social distancing affects the spread of the virus in each case. Chapter 3 examines the effects of social distancing by introducing a threshold based on the total number of infected individuals, providing insight into how such measures influence the course of an epidemic. In Chapter 4, we extend this analysis by modeling individuals as nodes within a network. We then study how social distancing impacts the spread of infection across two different network structures under both scenarios.

3 Epidemic patterns of emerging variants with dynamical social distancing

Motivated by the emergence of new variants during the COVID-19 pandemic, we investigate an epidemiological model of disease transmission dynamics that incorporates the appearance of novel strains through virus mutations. In our analysis, social distancing measures significantly influence the prevalence of the disease within the population. We explore various patterns that arise under different assumptions regarding cross-immunity. If recovery from a specific strain provides immunity against all previous strains but not against newer ones, we observe a consistent sequential pattern of strain replacement, with newer strains prevailing over older ones. However, if immunity upon recovery is strain-specific, without protection against other strains, we observe more intricate dynamics, including the potential recurrence of earlier strains and the co-circulation of multiple strains. We compare these observed patterns with genomic analyses conducted during the COVID-19 pandemic in the Netherlands.

In [48], the authors investigated the evolution of resistance to COVID-19 vaccination in the presence of social distancing. They derived a formula for the probability of the emergence of vaccine resistance over time for a model with two strains: WT (wild-type virus) and a vaccine-resistant mutant virus (MT). In their simulations, the social activity level (contact numbers) is adjusted such that the number of infected individuals remains constant over time (i.e., the effective reproduction number is modulated to one). They found that under slow vaccination, resistance is more likely to emerge even if social distancing is maintained, while in the case of rapid vaccination, the emergence of mutants can be prevented if social distancing is observed during vaccination.

In this chapter, we develop a model similar to existing frameworks, but with an added dimension: the emergence of n ($n \in \mathbb{N}$) new strains through mutations. Our primary objective is to explore emerging dynamics, particularly focusing on cross-immunity patterns between strains, while considering the influence of dynamically changing social distancing measures.

The structure of our work is as follows: Section 3.1 provides an overview of our general model. We present two distinct scenarios within this model. The first

scenario, detailed in Section 3.2, assumes one-way cross-immunity, where recovered individuals develop immunity against the strain that infected them and all preceding strains, yet remain susceptible to newly emerging strains. We compute the time-varying effective reproduction number for each strain (Subsection 3.2.3) and analyze the patterns observed in consecutive waves through numerical simulations.

In Section 3.3, we introduce and contrast the second scenario with the first. In this scenario, recovered individuals acquire immunity solely against the strain that infected them, while remaining susceptible to both new and prior strains. This leads to more intricate dynamics compared to the first scenario.

Finally, in Section 3.4, we compare our findings with data on COVID-19 variants in the Netherlands, providing insights and implications drawn from our model's predictions.

3.1 Model Description

We construct a compartmental model to describe a general model of an infectious disease with multiple variants. In our model, the population N is divided into the following three main classes, tracking the disease status of individuals: S denotes susceptible individuals; I denotes infected individuals; and R represents the population of recovered individuals. This classical SIR-setting is extended to accommodate multiple strains. We use the notation I_k for the class of individuals infected by strain k ($k = 1, 2, \ldots, n$). Upon recovery, individuals move to compartment R_k. As a simplification, individuals in R_k are those who recovered from infection k, and they all possess the same type of immunity, regardless of whether they may have been infected in the past by other strains. The model neglects any changes in the population due to birth, death, or migration during the period under consideration. Thus, the total population (N) remains invariant for all t.

$$S(t) + \sum_{k=1}^{n} (I_k(t) + R_k(t)) = N.$$

We introduce the general cross-immunity matrix $C = c_{ij}$ $(i, j = 1, 2, \ldots, n)$ as the relative immunity to strain i after recovering from strain j and transitioning into the R_j state. With this notation, $c_{ij} = 0$ denotes full immunity of R_j individuals to strain i, while $c_{ij} = 1$ indicates no immunity at all (full susceptibility) to the strain. If the value of c_{ij} is between 0 and 1, then there is partial immunity to strain i. In the model equations, the coefficients c_{ij} will appear as a reduction factor in the transmission rate between compartments R_j and I_i. The strains are assumed to share the same epidemiological parameters (transmission and recovery rates); they only differ in terms of population immunity against them.

The proposed model is governed by the following system of differential equations:

$$
\begin{aligned}
\dot{S}(t) &= -\beta\sigma(t)S(t)\sum_{i=1}^{n} I_i(t),\\
\dot{I}_1(t) &= \beta\sigma(t)(1-\alpha)S(t)I_1(t) + \beta\sigma(t)(1-\alpha)I_1(t)\sum_{i=1}^{n} c_{1,i}R_i(t) - \gamma I_1(t),\\
\dot{R}_1(t) &= \gamma I_1(t) - \beta\sigma(t)R_1(t)\sum_{i=1}^{n} c_{i,1}I_i(t),\\
&\vdots\\
\dot{I}_k(t) &= \beta\sigma(t)(1-\alpha)S(t)I_k(t) + \beta\sigma(t)\alpha S(t)I_{k-1}(t) - \gamma I_k(t)\\
&\quad + \beta\sigma(t)(1-\alpha)I_k(t)\sum_{i=1}^{n} c_{k,i}R_i(t) + \beta\sigma(t)\alpha I_{k-1}(t)\sum_{i=1}^{n} c_{k-1,i}R_i(t), \qquad (3.1)\\
\dot{R}_k(t) &= \gamma I_k(t) - \beta\sigma(t)R_k(t)\sum_{i=1}^{n} c_{i,k}I_i(t),\\
&\vdots\\
\dot{I}_n(t) &= \beta\sigma(t)\alpha S(t)I_{n-1}(t) + \beta\sigma(t)S(t)I_n(t) - \gamma I_n(t)\\
&\quad + \beta\sigma(t)I_n(t)\sum_{i=1}^{n} c_{n,i}R_i(t) + \beta\sigma(t)\alpha I_{n-1}(t)\sum_{i=1}^{n} c_{n-1,i}R_i(t),\\
\dot{R}_n(t) &= \gamma I_n(t) - \beta\sigma(t)R_n(t)\sum_{i=1}^{n} c_{i,n}I_i(t).
\end{aligned}
$$

where $k = 2, 3, \ldots, n-1$.

In the given system, parameters β and γ represent the average transmission rate and recovery rates, respectively. In this model, a mutation occurs with a small probability α when exposure to an infected individual with strain i results in transmission of strain $i+1$. Thus, mutations are assumed to be sequential, generating the subsequent variant ($i = 1, 2, \ldots, n$). Additionally, individuals recovered from strain i are assumed to be fully protected from strain I_i but susceptible or immune to others, as determined by the elements of matrix C.

In System 3.1, the parameter $\sigma = \sigma(t)$ represents a time-varying social distancing measure, ranging from 0 to 1, indicating the reduction in contacts compared to baseline. A value of $\sigma = 1$ implies no social distancing, while $\sigma = 0$ indicates complete lockdown. Social distancing plays a crucial role in controlling the infected population within acceptable limits. Denoted by L, the daily new infection threshold, $\sigma(t)$ is adjusted to ensure that the infectious population does not exceed L/γ. (Refer to Table 3.1 for parameter details.)

In the following, we explore two scenarios for matrix C: (i) if recovery from strain i provides immunity against previous strains, C is a triangular matrix (Section 3.2),

and (ii) if recovery from strain i confers immunity only against strain i, individuals remain susceptible to earlier and subsequent strains, then matrix C is 0 in the diagonal, and 1 in all off-diagonal elements (Section 3.3).

Parameter	Interpretation	Values
β	Transmission rate	7.5×10^{-7}
γ	Recovery rate (day^{-1})	0.25
α	Mutation probability	10^{-6}
σ	Social distancing parameter (reduction in contacts)	$[0, 1]$
N	Total population	10^6
L	Number of daily new infected (allowed incidence)	$900, 1500, 3500$

Table 3.1: *Parameters and values applied in the simulations. The parameters are set to give* $R_0 = 3$.

3.2 First Scenario: One-Way Cross-Immunity Towards Earlier Variants

3.2.1 Model Equations and the Cross-Immunity Matrix

In this scenario, individuals who have recovered from strain j ($j = 1, 2, \ldots, n$) are fully immune to any strain i where $i \leq j$, but they have no immunity to subsequent strains. The cross-immunity matrix C reflects this condition. For example, a recovered individual from strain two is immune to strain two and all preceding strains ($c_{i,2} = 0$, $i = 1, 2$), but remains susceptible to new strains, therefore can be infected by them at the same rate as susceptible individuals ($c_{i,2} = 1$, $i = 3, \ldots, n$). Hence,

$$C_{n,n} = \begin{pmatrix} 0 & 0 & 0 & \cdots & 0 \\ 1 & 0 & 0 & \cdots & 0 \\ 1 & 1 & 0 & \cdots & 0 \\ \vdots & \vdots & \vdots & \ddots & \vdots \\ 1 & 1 & 1 & \cdots & 0 \end{pmatrix}$$

is a lower triangular cross-immunity matrix, with zeros on the diagonal.

In order to derive the model equations, the following assumptions are considered:

- Each strain can infect susceptible individuals S.

- Recovered individuals from strain j are susceptible to strain i, where $i > j$, and immune to previous ones.
- Individuals infected by strain i can transmit strain $i+1$ due to mutation with a mutation probability μ.

Based on these assumptions, the system of differential equations for the model is given by:

$$
\begin{aligned}
\dot{S}(t) &= -\beta\sigma(t)S(t)\sum_{i=1}^{n} I_i(t),\\
\dot{I}_1(t) &= \beta\sigma(t)(1-\alpha)S(t)I_1(t) - \gamma I_1(t),\\
\dot{R}_1(t) &= \gamma I_1(t) - \beta\sigma(t)R_1(t)\sum_{i=2}^{n} I_i(t),\\
&\vdots\\
\dot{I}_k(t) &= \beta\sigma(t)(1-\alpha)S(t)I_k(t) + \beta\sigma(t)\alpha S(t)I_{k-1}(t) - \gamma I_k(t)\\
&\quad + \beta\sigma(t)(1-\alpha)I_k(t)\sum_{i=1}^{k-1} R_i(t) + \beta\sigma(t)\alpha I_{k-1}(t)\sum_{i=1}^{k-2} R_i(t), \qquad (3.2)\\
\dot{R}_k(t) &= \gamma I_k(t) - \beta\sigma(t)R_k(t)\sum_{i=k+1}^{n} I_i(t),\\
&\vdots\\
\dot{I}_n(t) &= \beta\sigma(t)\alpha S(t)I_{n-1}(t) + \beta\sigma(t)S(t)I_n(t) - \gamma I_n(t)\\
&\quad + \beta\sigma(t)I_n(t)\sum_{i=1}^{n-1} R_i(t) + \beta\sigma(t)\alpha I_{n-1}(t)\sum_{i=1}^{n-2} R_i(t),\\
\dot{R}_n(t) &= \gamma I_n(t)
\end{aligned}
$$

where $k = 2, 3, \ldots, n-1$.

3.2.2 Epidemiological Dynamics

We have numerically solved System (3.2), and Fig. 3.1 displays the number of infected individuals over time for each strain. Initially, we assume a population of $N = 10^6$, with 1000 individuals infected by strain 1. In the early stage of the epidemic, no social distancing measures are in place ($\sigma = 1$). Subsequently, when the infected population reaches a threshold of L/γ (corresponding to a daily incidence of L), we implement social distancing measures to stabilize the infected population at this fixed level, $\sum_{j=1}^{n} I_j = L/\gamma$. Under this assumption, the effective reproduction number during these periods is equal to one (it will be explained in detail in the next subsection). As the number of infections from the initial strain diminishes due to recoveries, the newly emerged strains will sequentially replace the previous ones in

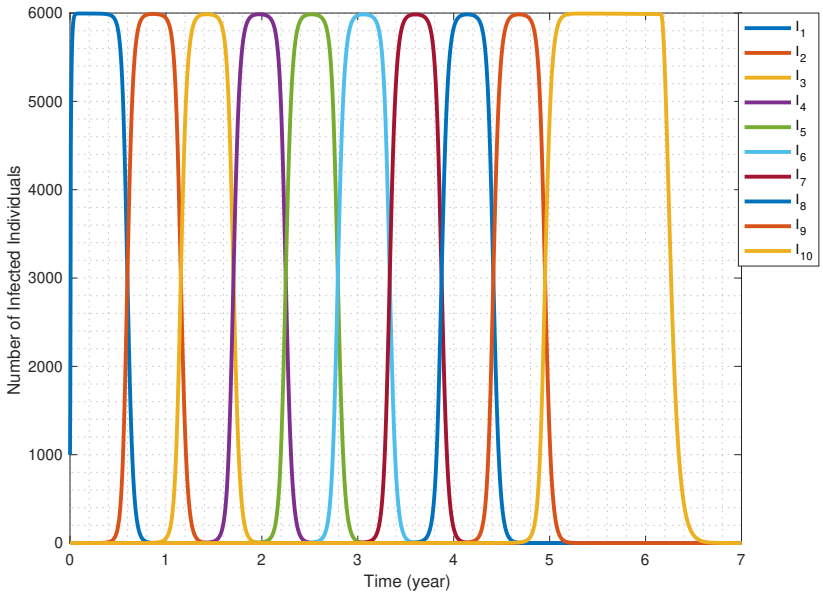

Figure 3.1: *Infections behavior over time of Scenario 1;* $N = 10^6$, $L = 1500$, $\gamma = 0.25$, $\beta = 7.5 \times 10^{-7}$.

dominance. This transition is evident in Fig. 3.1, where the emerging strains have a similar slope to the old declining strains.

Fig. 3.2 illustrates the impact of the daily number of allowable new infections on the implementation of social distancing measures over time: a higher number of newly infected individuals per day corresponds to a higher $\sigma(t)$, indicating milder interventions for social distancing. It is also noticeable that as a dominant strain wanes, we can relax the measures to some extent. However, as new strains emerge and gain prominence, stricter measures become necessary once again, leading to an oscillatory pattern in the intensity of interventions.

Looking at Fig. 3.1, a natural question arises: do newer strains exhibit the same dominance period as earlier ones, given their similar appearance on the graph? To address this, we compare the dominance periods of each strain within the population across three different values of L. The interesting outcome is depicted in Fig. 3.3.

This figure illustrates that allowing more new individuals to be infected by a strain results in a shorter duration of dominance and quicker fade-out of that strain. To compute the dominance period of a variant in the population, we measure the time difference when the number of infected individuals with each strain reaches $L/(2\gamma)$. As observed in Fig. 3.1, the number of people infected with strain i $(i = 1, 2, \ldots, n)$ reaches $L/(2\gamma)$ at two distinct times: when strain i is emerging (while strain $i - 1$ is dying out) and when it is fading out (while strain $i + 1$ is emerging). Thus, the dominance period is defined as the time difference between these two points, representing the duration for a strain to maintain a higher number of infections than $L/(2\gamma)$. As illustrated in Fig. 3.3, under this scenario, each subsequent strain exhibits

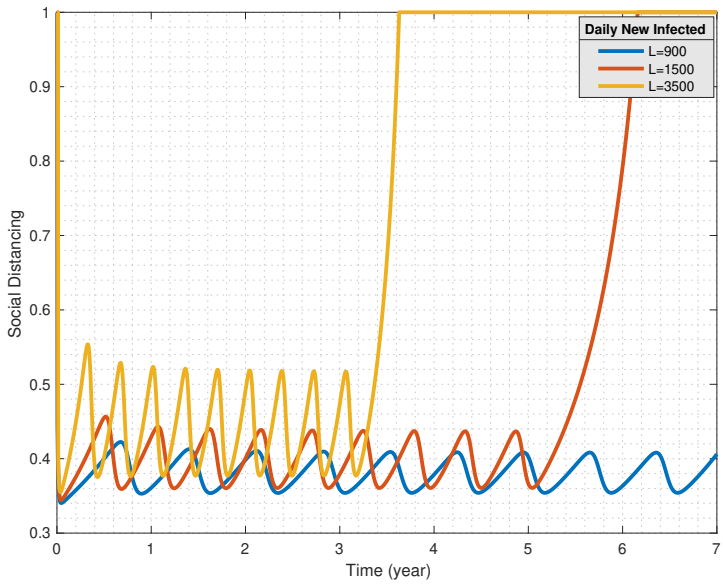

Figure 3.2: *Relation between social distancing parameter, $\sigma(t)$, and L for ten strains of the first scenario.*

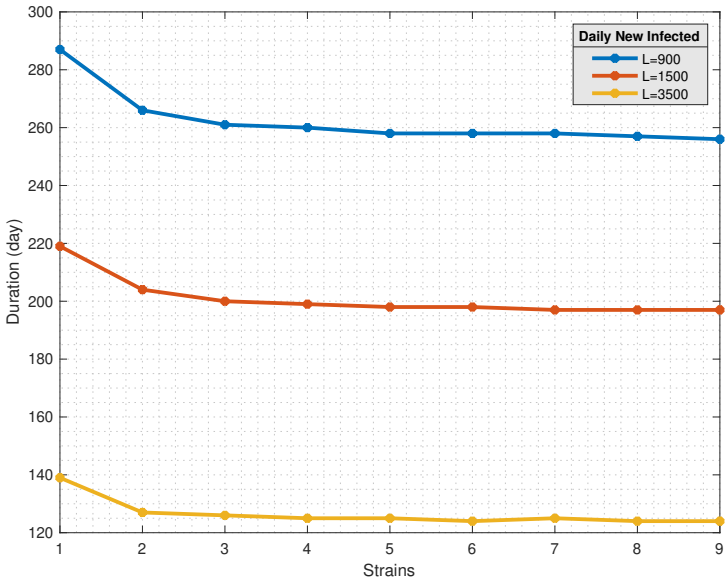

Figure 3.3: *Relation between new infections per day $(L(t))$ and duration of persistence in the population.*

a shorter period of dominance compared to the previous ones. Conversely, a higher allowed incidence corresponds to shorter dominance periods and a faster emergence of novel strains.

3.2.3 Reproduction Numbers

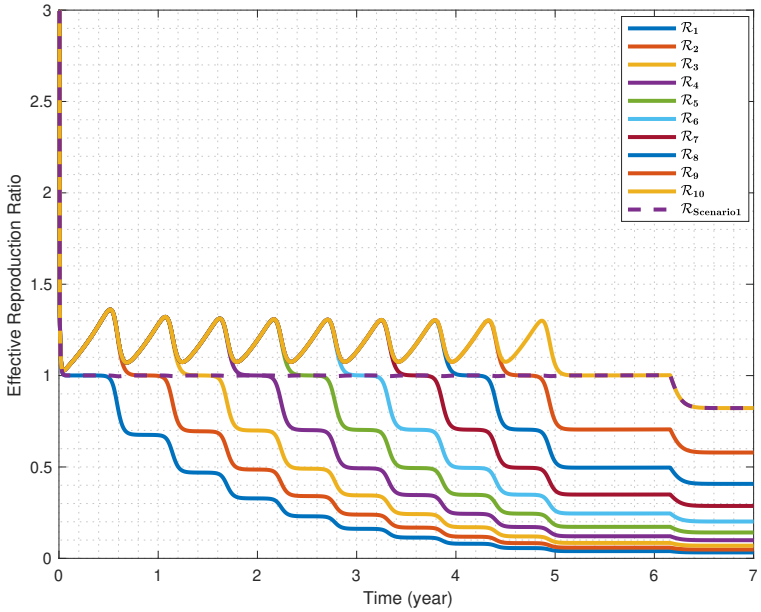

Figure 3.4: *Effective reproduction number for each strain of System 3.1.*

Fig. 3.4 illustrates the effective reproduction number for each strain over time. Initially, all strains have the potential to infect the entire population. However, as time progresses, each strain infects fewer individuals due to recovery from the infection caused by that strain. Despite this, new mutations can still potentially infect every individual in the population, as recovered individuals from previous strains remain susceptible to new ones.

According to our basic assumption, the social distancing parameter is manipulated to maintain a fixed number of infected individuals ($\sum_{j=1}^{n} I_j = L/\gamma$), resulting in an effective reproduction number of 1 for Model 1 (depicted by the dashed line in Fig. 3.4).

The overall effective reproduction number is calculated as the weighted average of all strain reproduction numbers, where the weights are determined by the number of infected individuals for each strain. Specifically, to compute these reproduction numbers, we construct the next-generation matrix FV^{-1}, where matrices F and V are defined as described by [80]:

Let $I = (I_1, I_2, \ldots, I_n)^T$ denote the number of individuals in infection compartments in System (3.2). We express the corresponding equations in the form of

$\dot{I}_i = \mathcal{F}_i(I) - \mathcal{V}_i(I)$ for $i = 1, 2, \ldots, n$, where $\mathcal{F}_i$ represents the appearance of new infections in compartment i, and $\mathcal{V}_i$ denotes the rate of transitions between compartment i and other infected compartments. We define the non-negative matrix $F = \frac{\partial \mathcal{F}_i(I)}{\partial I_j}$ and the non-singular matrix $V = \frac{\partial \mathcal{V}_i(I)}{\partial I_j}$ for $1 \leq i, j \leq n$. This formulation yields:

$$F_{n,n} = \begin{pmatrix} (1-\alpha)\bar{A}_1 & 0 & 0 & \cdots & 0 & 0 \\ \alpha\bar{A}_1 & (1-\alpha)\bar{A}_2 & 0 & \cdots & 0 & 0 \\ 0 & \alpha\bar{A}_2 & (1-\alpha)\bar{A}_3 & \cdots & 0 & 0 \\ 0 & 0 & \alpha\bar{A}_3 & \cdots & 0 & 0 \\ \vdots & \vdots & \vdots & \ddots & \vdots & \vdots \\ 0 & 0 & 0 & \cdots & \alpha\bar{A}_{n-1} & \bar{A}_n \end{pmatrix},$$

and

$$V_{n,n} = \begin{pmatrix} a & 0 & 0 & \cdots & 0 \\ 0 & a & 0 & \cdots & 0 \\ 0 & 0 & a & \cdots & 0 \\ \vdots & \vdots & \vdots & \ddots & \vdots \\ 0 & 0 & 0 & \cdots & a \end{pmatrix},$$

where $\bar{A}_1 = \beta\sigma S$ and $\bar{A}_i = \beta\sigma(S + \sum_{k=1}^{i-1} R_k)$ for $i = 2, 3, \ldots, n$. At the next step, we generate the next generation matrix FV^{-1} as

$$FV^{-1}{}_{n,n} = \begin{pmatrix} \frac{(1-\alpha)\bar{A}_1}{\gamma} & 0 & 0 & \cdots & 0 & 0 \\ \frac{\alpha\bar{A}_1}{\gamma} & \frac{(1-\alpha)\bar{A}_2}{\gamma} & 0 & \cdots & 0 & 0 \\ 0 & \frac{\alpha\bar{A}_2}{\gamma} & \frac{(1-\alpha)\bar{A}_3}{\gamma} & \cdots & 0 & 0 \\ \vdots & \vdots & \vdots & & \vdots & \vdots \\ 0 & 0 & 0 & \ldots & \frac{\alpha\bar{A}_{n-1}}{\gamma} & \frac{\bar{A}_n}{\gamma} \end{pmatrix}.$$

The eigenvalues of the next-generation matrix provide the effective reproduction numbers for each strain, which vary over time. The eigenvalues

$$\mathcal{R}(1) = \frac{(1-\alpha)\beta\sigma(t)S(t)}{\gamma}$$

and

$$\mathcal{R}(n) = \frac{\beta\sigma(t)\left(S(t) + \sum_{k=1}^{n-1} R_k(t)\right)}{\gamma}$$

are effective reproduction numbers corresponding to the first and last strains, respectively, and

$$\mathcal{R}(i) = \frac{(1-\alpha)\beta\sigma(t)\left(S(t) + \sum_{k=1}^{i-1} R_k(t)\right)}{\gamma}$$

is the effective reproduction number for infection compartments I_i, $i = 2, 3, \ldots, n-1$.

Moreover, the overall effective reproduction number for the first scenario of our model can be calculated as:

$$\mathcal{R}_{\text{Scenario1}} = \frac{\sum_{j=1}^{n} I_j(t)\mathcal{R}(j)}{\sum_{j=1}^{n} I_j(t)}.$$

It is important to note that in general, the next-generation matrix is calculated at a steady state. However, to determine the effective reproduction numbers at every time point t, we freeze the values of $S(t)$, $\sigma(t)$, and $R_k(t)$ for the duration in which the subsequent infected generation is being created. This approach allows us to ignore short-term changes in these values and treat them as steady states, enabling us to perform the same formal calculations as in the classical case.

3.3 Second Scenario: Absence of Cross-Immunity

3.3.1 Model Equations and the Cross-Immunity Matrix

Let us now consider a scenario where protection upon recovery from one strain provides immunity only against that particular strain. In this scenario, individuals who have recovered from a specific strain remain susceptible to both old and new strains. This is reflected in the cross-immunity matrix, where only the diagonal elements are zero, indicating full immunity to the recovered strain, while all other elements are one, signifying no protection against other strains. Thus, the cross-immunity matrix can be defined as follows:

$$C_{n,n} = \begin{pmatrix} 0 & 1 & 1 & \cdots & 1 \\ 1 & 0 & 1 & \cdots & 1 \\ 1 & 1 & 0 & \cdots & 1 \\ \vdots & \vdots & \vdots & \ddots & \vdots \\ 1 & 1 & 1 & \cdots & 0 \end{pmatrix}.$$

The second scenario is based on the following assumptions:

- Each strain can infect susceptible individuals S.
- Recovered individuals from strain i are only resistant to this strain and not protected against other strains.
- Individuals infected by strain i can transmit strain $i+1$ due to mutation.

The dynamics of the epidemic model we described can be summarized by the following equations for $k = 2, 3, \ldots, n-1$:

$$\begin{aligned}
\dot{S}(t) &= -\beta\sigma(t)S(t)\sum_{i=1}^{n} I_i(t), \\
\dot{I}_1(t) &= \beta\sigma(t)(1-\alpha)S(t)I_1(t) + \beta\sigma(t)(1-\alpha)I_1(t)\sum_{i=2}^{n} R_i(t) - \gamma I_1(t), \\
\dot{R}_1(t) &= \gamma I_1(t) - \beta\sigma(t)R_1(t)\sum_{i=2}^{n} I_i(t), \\
&\vdots \\
\dot{I}_k(t) &= \beta\sigma(t)(1-\alpha)S(t)I_k(t) + \beta\sigma(t)\alpha S(t)I_{k-1}(t) - \gamma I_k(t) \\
&\quad + \beta\sigma(t)(1-\alpha)I_k(t)\sum_{i=1, i\neq k}^{n} R_i(t) + \beta\sigma(t)\alpha I_{k-1}(t)\sum_{i=1, i\neq k-1}^{n} R_i(t), \\
\dot{R}_k(t) &= \gamma I_k(t) - \beta\sigma(t)R_k(t)\sum_{i=1, i\neq k}^{n} I_i(t), \\
&\vdots \\
\dot{I}_n(t) &= \beta\sigma(t)\alpha S(t)I_{n-1}(t) + \beta\sigma(t)S(t)I_n(t) - \gamma I_n(t) \\
&\quad + \beta\sigma(t)I_n(t)\sum_{i=1}^{n-1} R_i(t) + \beta\sigma(t)\alpha I_{n-1}(t)\sum_{i=1, i\neq n-1}^{n} R_i(t), \\
\dot{R}_n(t) &= \gamma I_n(t) - \beta\sigma(t)R_n(t)\sum_{i=1}^{n-1} I_i(t).
\end{aligned} \tag{3.3}$$

3.3.2 Epidemiological Dynamics

In this case, unlike in Scenario 1, recovered individuals are not immune to old variants. Consequently, the behavior of the infected populations in Fig. 3.5 is not as regular as those in Fig. 3.1.

As depicted in Fig. 3.5, for each strain, the infections settle around the value $L/\gamma n$ over time. In other words, for large t, we have:

$$I_i(t) \approx \frac{L}{\gamma n}, \qquad i = 1, 2, \ldots, n.$$

This phenomenon can be intuitively explained as follows: In the first scenario, susceptibility is limited to the new strains only, meaning recovered individuals cannot be infected with old strains, and there is no mutation from new strains to previous ones. Consequently, the earlier strains cannot compete with newer ones and converge to zero, while the new ones rise to L/γ.

However, in Scenario 2, each strain infects all recovered individuals, who have recovered from both new and old strains (except from the very same strain), equalizing their potential pools. Moreover, the total number of infected individuals is constrained to L/γ, which is now distributed among n equally competitive strains.

As a result, the effective reproduction numbers hover around one, since the number of infected individuals neither increases nor decreases during these times (see Fig. 3.6).

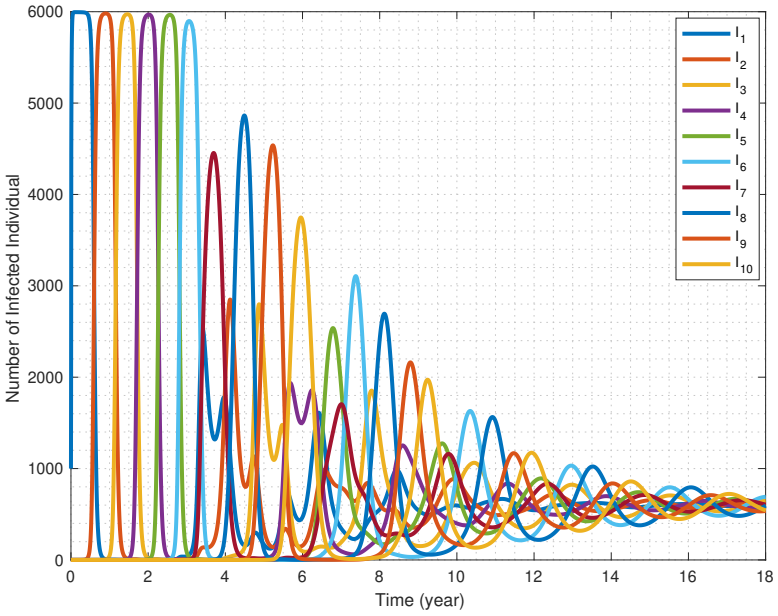

Figure 3.5: *Infected population of each strain of Scenario 2, that are approaching* $L/(\gamma n)$.

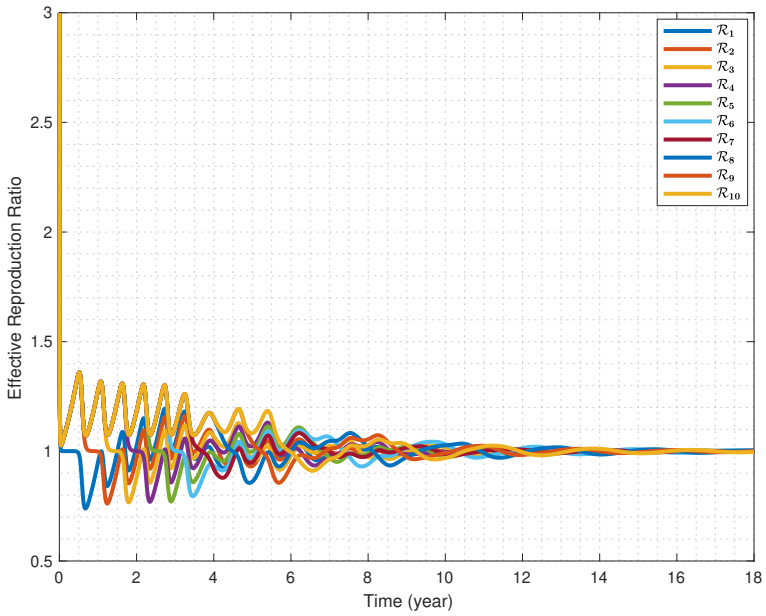

Figure 3.6: *Effective reproduction numbers for each strain approach one as the infected population approaches* $L/(\gamma n)$.

3.3.3 Effective Reproduction Numbers

To determine the effective reproduction number for each strain in this scenario, we follow the procedure outlined in Subsection 3.2.3: first, we construct the next-generation matrix, and then we compute its eigenvalues, which correspond to the effective reproduction numbers for each strain.

We express the equations for the infected compartments $I = (I_1, I_2, \ldots, I_n)^T$ in System 3.3 as

$$\dot{I}_i = \mathcal{F}_i(I) - \mathcal{V}_i(I), \quad i = 1, 2, \ldots, n.$$

Here, $\mathcal{F}_i$ and $\mathcal{V}_i$ are defined in the same manner as described in Subsection 3.2.3. We define the non-negative matrix $F = \frac{\partial \mathcal{F}_i(I)}{\partial I_j}$ and the non-singular matrix $V = \frac{\partial \mathcal{V}_i(I)}{\partial I_j}$ for $1 \leq i, j \leq n$ as follows:

$$F_{n,n} = \begin{pmatrix} (1-\alpha)B_1 & 0 & 0 & \cdots & 0 & 0 \\ \alpha B_1 & (1-\alpha)B_2 & 0 & \cdots & 0 & 0 \\ 0 & \alpha B_2 & (1-\alpha)B_3 & \cdots & 0 & 0 \\ 0 & 0 & \alpha B_3 & \cdots & 0 & 0 \\ \vdots & \vdots & \vdots & \ddots & \vdots & \vdots \\ 0 & 0 & 0 & \cdots & \alpha B_{n-1} & B_n \end{pmatrix},$$

$$V_{n,n} = \begin{pmatrix} \gamma & 0 & 0 & \cdots & 0 \\ 0 & \gamma & 0 & \cdots & 0 \\ 0 & 0 & \gamma & \cdots & 0 \\ \vdots & \vdots & \vdots & \ddots & \vdots \\ 0 & 0 & 0 & \cdots & \gamma \end{pmatrix},$$

where $B_i = \beta\sigma(S + \sum_{k=1\neq i}^{n} R_k)$ for $i = 1, 2, \ldots, n$. Then we create the matrix FV^{-1}

$$FV^{-1}{}_{n,n} = \begin{pmatrix} \frac{(1-\alpha)B_1}{\gamma} & 0 & 0 & \cdots & 0 & 0 \\ \frac{\alpha B_1}{\gamma} & \frac{(1-\alpha)B_2}{\gamma} & 0 & \cdots & 0 & 0 \\ 0 & \frac{\alpha B_2}{\gamma} & \frac{(1-\alpha)B_3}{\gamma} & \cdots & 0 & 0 \\ \vdots & \vdots & \vdots & & \vdots & \vdots \\ 0 & 0 & 0 & \cdots & \frac{\alpha B_{n-1}}{\gamma} & \frac{B_n}{\gamma} \end{pmatrix}.$$

The eigenvalues of this matrix give us the effective reproduction numbers for each strain. In particular, the eigenvalue

$$\mathcal{R}(n) = \frac{\beta\sigma(t)(S(t) + \sum_{k=1}^{n-1} R_k(t))}{\gamma}$$

is the effective reproduction number that corresponds to the last strain, and

$$\mathcal{R}(i) = \frac{(1-\alpha)\beta\sigma(t)(S(t) + \sum_{k=1\neq i}^{n} R_k(t))}{\gamma}$$

is the effective reproduction number corresponding to strain i, $i = 1, 2, \ldots, n-1$.

3.4 Discussion

The emergence and persistence of novel mutations in infectious diseases, particularly COVID-19, necessitate the implementation of a general model incorporating multiple strains emerging through mutations. For simplicity, we assume that the strains share identical epidemiological parameters, differing only in the target populations they can infect, as determined by a cross-immunity matrix. In this chapter, we consider two scenarios focusing on immune evasion by newer strains resulting from virus mutations.

In the first scenario, recovery from a strain confers full protection against previous strains but provides no immunity to novel strains. Simulation results reveal a highly structured sequential pattern of strain replacement, where newer strains predominate over older strains but persist in the population for increasingly shorter periods.

Conversely, in the second scenario, immunity upon recovery is specific to a given strain and does not confer immunity against others. As a result, the population infected by each strain exhibits an erratic pattern over time, with recurrence of past strains and co-circulation of multiple strains without clear dominance.

In the following example, we compare our model results with reported data on SARS-CoV-2 variants in the Netherlands.

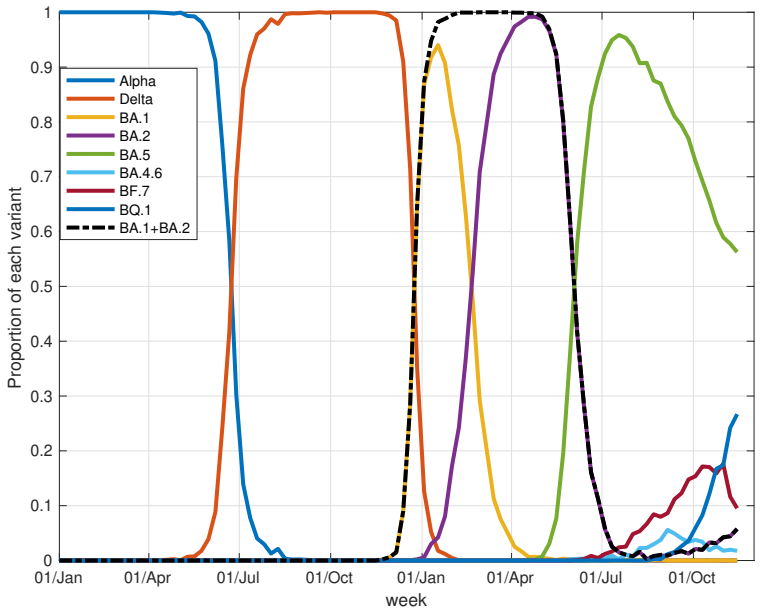

Figure 3.7: *Variants of the coronavirus SARS-COV-2 in the Netherlands from* $30/11/2020$ *to* $14/12/2022$.

Fig. 3.7 illustrates the frequency of COVID-19 variants in the Netherlands during 2021–2022, based on data from [70]. The graph depicts the emergence and dom-

inance of variants Alpha and Delta, which closely mirrors the patterns observed in Scenario 1 of our model. Notably, the durations of dominance for these variants exhibit striking similarities between the model and the empirical data. However, starting from June 2022, a significant shift occurs, with the Omicron lineage accounting for the majority of SARS-CoV-2 variants. Within the Omicron lineage, sub-variants such as BA.5 remain prevalent, while newer sub-variants like BQ.1 are on the rise.

The emergence of these Omicron sub-variants is cause for concern, as they have been shown to possess immune-evading properties [82]. This could potentially undermine the efficacy of current COVID-19 vaccines and compromise existing natural immunity, leading to increased rates of infections and reinfections. This evolving situation bears resemblance to Scenario 2 in our model, where irregular circulation patterns are observed over time, akin to the fluctuations depicted in Fig. 3.5 and reflected in the Netherlands data shown in Fig. 3.7. These parallels affirm that our model captures essential aspects of variant dynamics observed during the course of the COVID-19 pandemic.

4 Modeling Network Epidemics with Mutation and Cross-Immunity: A Stochastic Approach

Exploring scenarios concerning the mutation and immunity of viral strains has become crucial to understanding the different patterns of virus spread. This chapter gains insight into the application of continuous-time stochastic epidemic models on network structures, focusing on the SIR framework to simulate and analyze these scenarios. By examining the effects of viral mutations and cross-immunity, this study shifts its attention from the broader dynamics of disease spread across various network models to the nuanced interactions between viral evolution and immune response, using the Gillespie algorithm for the simulations.

4.1 Introduction to Network Science in Epidemiology

Networks offer a natural way to represent systems made up of many interacting parts. In the context of infectious disease modeling, individuals can be represented as nodes and their contacts as edges in a network. This approach helps capture the structure of real-world interactions and has become widely used across many fields, including epidemiology, biology, computer science, and social sciences.

Using real contact network data and a careful analysis of how diseases spread through populations, researchers have shown that networks can provide important insights that simpler models may miss. Traditional models like the well-mixed SIR assume that everyone in a population mixes randomly. While this assumption simplifies analysis and often works well for large, homogeneous populations, it can overlook important details about how people actually interact. For example, people do not all have the same number of contacts, and some interactions—like those within households or between close partners—can last much longer than others. These differences matter for how diseases spread. In particular, the duration of partnerships can have a strong influence on transmission, especially for infections that require close or prolonged contact, such as respiratory or sexually transmitted diseases.

Network-based models take these factors into account by representing individuals and their specific contacts directly. This makes it possible to study how local patterns of interaction affect the timing and size of outbreaks, as well as the impact of immu-

nity and viral mutation. These models are especially useful when studying smaller communities, or when individual variation in contact patterns plays a major role in transmission.

4.1.1 A Framework for Simulating Epidemics on Networks

In this work, we use a network-based SIR model to study how infectious diseases spread through structured populations. The simulations are carried out using continuous-time stochastic processes, with the Gillespie algorithm used to model the random timing of infection and recovery events.

Unlike classical models that assume random mixing across the entire population, network models make the contact structure explicit. Here, each node represents an individual, and edges represent fixed connections through which infection can pass. The main type of variation considered in this framework is the number and arrangement of these contacts.

One important difference between network and well-mixed models is how they handle the depletion of susceptible individuals. Classical well-mixed models assume that every individual in the population has an equal chance of coming into contact with any other, regardless of location or social structure. As a result, they treat the depletion of susceptible individuals as a global process—susceptibles are assumed to be removed evenly across the population as the epidemic progresses. This leads to the assumption that, early in the epidemic, each infected individual is surrounded by a fully susceptible neighborhood, which can result in an overestimation of the early spread of the disease.

In contrast, infections in real-world contact networks often occur in localized clusters. Once an infected individual has transmitted the disease to their nearby contacts, the local pool of susceptibles is quickly reduced, slowing the spread in that area. Well-mixed models do not capture this effect, leading to faster-than-realistic early growth.

Later in the epidemic, individuals who are infected at later stages may belong to parts of the network that have not yet been exposed to the disease. Their surrounding contacts may still be largely susceptible, allowing transmission to continue even when the total number of susceptibles in the population is relatively low. Since well-mixed models do not consider these local variations, their predictions may also become inaccurate in the later phases of an outbreak.

By modeling these effects directly, network-based approaches provide a more detailed view of how contact patterns shape the course of an epidemic. This is especially important when studying complex processes such as mutation and cross-immunity, which depend not only on who is infected, but also on how individuals are connected.

This recognition of spatial heterogeneity and complex interactions among individuals highlights the necessity for a more sophisticated approach to modeling epidemic spread. In this context, continuous-time stochastic epidemic models on network structures present a promising alternative. In these models, individuals are considered as *nodes*, and the interactions among them are illustrated through the *edges*

of the network. Within the SIR framework, each node is categorized into one of three states: susceptible (S), infected and infectious (I), or recovered/immune/removed (R). The dynamics (without demography) are primarily governed by two processes: (a) the transmission of infection across the edges of the network which is modeled as a Poisson process with a transmission rate β, and (b) recovery, which is independent of the network's structure and follows a Poisson process with a recovery rate γ (Fig. 4.1). Therefore, when a susceptible node has k infectious contacts, it becomes infected through a Poisson process with rate $k\beta$.

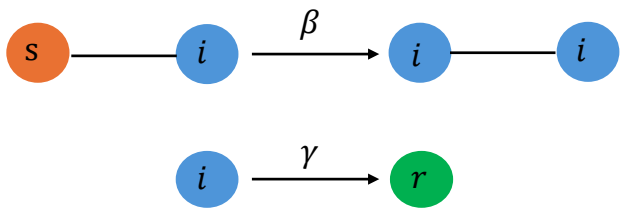

Figure 4.1: *In this SIR model, a susceptible node, who is in contact with an infected individual, will be infected at rate β. An infected node recovers with rate γ, independently of the status or number of their contacts.*

4.1.1.1 Stochastic simulation

The initial phase of exploring the stochastic dynamics of epidemic spread across a network involves individual-based stochastic simulations. This approach meticulously tracks every potential event and its occurrence rate within the network.

A common strategy for these simulations involves progressing through time in small increments Δt, which is not a fixed time step; rather, it is a random variable generated from an exponential distribution. Each infection event occurs at a specific time t, where an individual instantly transitions from the susceptible state to the infectious state. Such jumping processes occur according to Poisson processes [52]. One widely used and computationally efficient approach for simulating such processes is the Gillespie algorithm, also known as the stochastic simulation algorithm. This method includes two variants: the first reaction method and the direct method. In this work, we focus on the direct method and describe it in more detail. We will focus on the latter one and explain it more. In this algorithm for the SIR model, the Poisson processes are used to model the occurrences of events, such as transmission of infection and recovery, over time.

Deciphering Epidemics with the Gillespie Algorithm

The Gillespie algorithm plays a critical role in simulating the stochastic dynamics of epidemic spread. Below, we present a detailed pseudocode tailored to an SIR model in network contexts, where two events—infection and recovery—occur based on Poisson processes. The rate of infection is given by:

$$\beta \sum_{j=1}^{N} \sum_{i=1}^{N} S^i G_{ij} I^j \tag{4.1}$$

where β is the transmission rate, and $G = (G_{ij})$ is an adjacency matrix representing the network structure among N nodes (individuals). In this matrix, $G_{ij} = G_{ji} = 1$ if nodes i and j are connected, and $G_{ij} = 0$ otherwise. The state vectors $S = (S^1, \ldots, S^N)$ and $I = (I^1, \ldots, I^N)$ are binary indicators: $S^i = 1$ if node i is susceptible, and $I^i = 1$ if node i is infected; otherwise, the values are zero. The waiting times Δt between consecutive events in a Poisson process follow an exponential distribution. Specifically, Δt is drawn from: $\Delta t = -\frac{1}{\Lambda} \log(u)$, where $\Lambda = \lambda_1 + \lambda_2$ and $u \sim \mathcal{U}(0, 1)$, based on the *Superposition Theorem* [52]. Here, $\lambda_1 = \beta \sum_{j=1}^{N} \sum_{i=1}^{N} S^i G_{ij} I^j$, and $\lambda_2 = \gamma \sum_{i=1}^{N} I^i$ are the rate of infection and total recovery rate, respectively, with γ denoting the recovery rate per infected node.

Algorithm 1: SIR Network Gillespie Simulation Pseudocode

Input:
- N: Number of nodes in the network
- t_{end} : Maximum time to run the simulation
- β: Transmission rate per edge
- γ: Recovery rate per infected individual
- I_0: Initial list of infected nodes

Output:
- out: A list containing the number of Susceptible, Infected, and Recovered individuals at each time step

procedure SIR GILLESPIE SIMULATION
    Initialize random network G, Initialize time t to 0, transmission rate β, and recovery rate γ
    Set the initial state of nodes: Infected I, Susceptible S, Recovered R
    Record the initial state in out
    Define time points T to record the epidemic spread
    while there are infected nodes in the network **do**
        Calculate probability of each event (infection and recovery)
        Determine next time event Δt
        Call a random number and select the next event based on the events' probabilities
        if the event is an infection **then**
            Infect the susceptible node by randomly selecting one of its
                connected infectious neighbors, and update its state to infected
        else (if the event is recovery)
            Recover the infected node and update its state to Recovered
        end if
        Update counters for Infected, Susceptible, and Recovered nodes
        Record current state in out
    end while
    Plot the epidemic curve from out
end procedure

4.2 Understanding Network Topologies: Scale-Free and Random Spatial-Geometric network

To comprehend the spread of infectious diseases within different populations, it is pivotal to explore the structure of networks that represent these populations. Two fundamental types of random networks, Scale-Free networks (SF) and Random Spatial Geometric networks (RSG), offer contrasting perspectives on network topology and its impact on disease dynamics.

In a random spatial geometric network, nodes are positioned within a defined spatial domain, often arranged on a square lattice. This network model incorporates randomness in the spatial distribution of nodes while retaining the underlying geometric structure. Each node represents a distinct entity or location, and the edges between nodes are determined by proximity within a specified distance threshold r. This network finds applications in various fields, including telecommunications, transportation, and epidemiology, where spatial interactions play a crucial role in network dynamics and phenomena. For instance, in epidemiology, these networks are particularly valuable for understanding the patterns of disease transmission within communities, as they capture the spatial proximity between individuals and facilitate the exploration of disease spread pathways within geographic areas.

Scale-free networks, generated using models like the Barabási–Albert model [14], are widely used to explore how infectious diseases spread across populations. These networks are characterized by a small number of highly connected nodes, or hubs, and a large number of nodes with few connections. This structure mirrors the uneven contact patterns found in real-world settings, making scale-free networks especially useful for capturing the influence of individuals with high contact rates, often referred to as super-spreaders. By simulating infectious disease spread on scale-free networks, we can explore the impact of network topology on epidemic dynamics, identify key transmission pathways and hub nodes driving epidemic outbreaks, and evaluate the effectiveness of targeted control strategies aimed at disrupting disease transmission within highly connected sub-networks. Additionally, scale-free networks allow for the investigation of emergent phenomena such as the "small-world" effect, where short average path lengths facilitate rapid epidemic dissemination, and the "preferential attachment" mechanism, where new infections are preferentially acquired by highly connected individuals, influencing epidemic dynamics and control measures. This network offers insights into the complex interplay between network structure, individual behavior, and disease transmission, informing the development of more effective public health interventions and strategies for infectious disease control [15].

Fig. 4.2 provides a visual comparison of these two networks, illustrating our investigation into how the type of network influences the spread of infectious diseases. Both networks possess an equal number of connections and nodes: 400 nodes an expected degree of 6 for both networks. All simulations presented in this chapter are based on these two specific network structures, and all figures are plotted using the same graphs to ensure consistency throughout the analysis.

In the random spatial geometric network, nodes are uniformly distributed across a unit square lattice (size 1×1), with connections established between node pairs if the Euclidean distance between them is less than a specified neighborhood radius $r = 0.07$. Since the nodes are randomly placed, the grid resolution (i.e., the density of nodes) is not fixed, but instead depends on the number of nodes N. The value of $r = 0.07$ represents the maximum connection distance, and it influences how densely the network is connected. Smaller values of r will result in fewer connections, while larger values will create more densely connected networks.

For the Barabási–Albert model, we initialize with $m_0 = 3$ nodes and iteratively introduce one new node at each step, connecting it to $m = 3$ existing vertices selected with a probability proportional to the number of links those nodes already possess. All simulations in this chapter were conducted using these two types of networks.

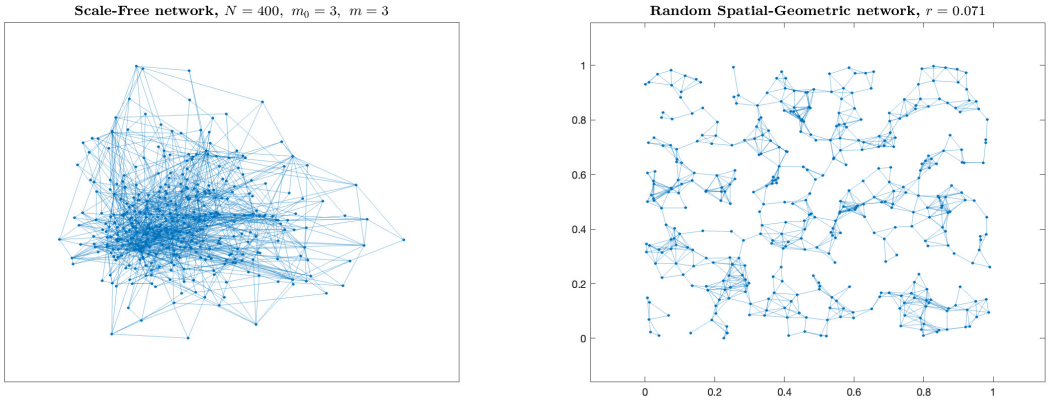

Figure 4.2: *Comparison of network models: Panel (a) depicts the scale-free network generated using the Barabási–Albert model, while panel (b) shows the random spatial-geometric network. Both networks consist of 400 nodes and 1200 edges. In the SF model, nodes are initialized with $m_0 = 3$ nodes and iteratively introduce one new node at each step, connecting it to $m = 3$ existing vertices selected with a probability proportional to the number of links those nodes already possess. In the RSG model, nodes are distributed across a square lattice, with connections established between nodes within a specified neighborhood radius $(r = 0.07)$ based on Euclidean distance.*

4.3 Case Study: Tracking Infectious Diseases Across Networks

This section investigates the spread of infectious diseases by comparing two distinct scenarios described in Chapter 3, involving the mutation and immunity of viral strains and analyzing the transmission dynamics across two different network structures. The primary aim is to understand how these scenarios and network topologies

collectively influence the patterns of disease spread and the effectiveness of interventions such as social distancing.

In both scenarios, the population is modeled as N nodes (individuals) within a randomly interconnected graph. The two network structures under consideration—SF and RSG—offer contrasting features in terms of connectivity and clustering, which significantly impact the transmission dynamics.

In these scenarios, viral strains are arranged in a circular network structure, where each strain is positioned on a unit circle at equal intervals. This circular layout is not only a topological feature of the mutation network (allowing strain k to mutate to strain 1 and vice versa), but it also encodes antigenic distance. Specifically, in our simulations, the antigenic distance $d_{ij} \in [0, 1]$ between strains is defined as the shortest arc length between two strain positions on a circle with circumference of length one. This formulation ensures circular continuity (e.g., strain 1 is adjacent to strain k), and captures the minimal antigenic separation in any direction around the circle. Mathematically, for strains located at positions p_i and p_j on the circle, we define:

$$d_{ij} = \min\left(|p_i - p_j|,\ 1 - |p_i - p_j|\right).$$

This distance modulates reinfection risk: the greater the distance between two strains, the more antigenically distinct they are. Accordingly, the infection rate is modified by including d_{ij} as a scaling factor in the reinfection term. For individuals with no prior exposure, d_{ij} is set to 1, corresponding to the maximum susceptibility, since they lack any prior immunity. In contrast, for previously infected individuals, d_{ij} reflects the antigenic similarity between the infecting strain and the previously encountered strain, with smaller values indicating greater similarity and thus stronger partial immunity.

In the first scenario, similar to the second scenario in the previous chapter (Section 3.3), viral strains exhibit dynamic mutation abilities, where each strain can either transition to a subsequent strain or revert to a previous one. This mutational flexibility is coupled with partial cross-immunity, meaning that recovery from one strain does not ensure immunity from other strains, particularly those that are antigenically distinct and connected within the network (i.e., there exists a direct connection or edge between them in the network model). In this scenario, d_{ij} is important because people can still get reinfected by other strains.

This scenario highlights the difficulty in predicting immunity, as individuals who recover from one strain may still be susceptible to other strains.

In this model, strains are arranged in a loop, so strain i can mutate both forward to strain $i + 1$ and backward to strain $i - 1$, with the circular structure allowing for a transition from the last strain k back to strain 1. This flexibility leads to the continuous circulation of various strains within the population. Similar to Fig. 3.5 from the previous chapter, in Fig. 4.3, the infected populations corresponding to adjacent strains converge over time, as strains share a common infectivity pool. The partial cross-immunity between antigenically distinct strains further facilitates reinfection cycles, perpetuating the circulation of multiple viral variants.

Conversely, the second scenario, which is similar to the one proposed in Section

3.2, presents a more linear mutation pattern, where each strain mutates strictly to the next in sequence. In this model, one-way cross-immunity is present, meaning that recovery from any given strain confers immunity to all preceding strains, but does not protect against strains that come after it in the mutation sequence. This setup reflects a more predictable and sequential progression of immunity, allowing for easier tracking of immunity acquisition across the population and potentially facilitating more effective management of outbreak dynamics. Even though cross-immunity moves in one direction and makes the spread more predictable, d_{ij} still matters by determining the reinfection risk from later strains that individuals have not yet encountered, with $d_{ij} = 0$ when $i > j$ due to full immunity to earlier strains.

In the second scenario, the strains are also arranged in a loop, but mutation occurs in only one direction: from strain i to strain $i + 1$, and the last strain k can mutate only to strain 1. This unidirectional mutation process leads to a sequential progression of immunity development, where each strain is gradually replaced by the next in line. As immunity builds up in the population, the pool of susceptible hosts for each subsequent strain decreases, leading to the eventual extinction of the strains. As shown in simulations (Fig. 4.4), each strain emerges, peaks, and then disappears as immunity builds against it, following a predictable sequence of infection.

In our stochastic SIR model, simulations begin with a single infection event: node 1 is initially infected with strain 1. To capture the intricate dynamics of the disease spread, we incorporate three crucial parameters:

- The transmission rate (β) determines the rate at which susceptible individuals contract the disease upon exposure to infected individuals. For our simulations, we set β to 0.1.

- The recovery rate (γ) represents the rate at which infected individuals recover from the disease and subsequently develop immunity. We assign γ a value of 0.08, indicating a moderate recovery rate consistent with typical disease progression dynamics, meaning that the average recovery time is $1/\gamma = 12.5$ days.

- Additionally, we define the mutation rate (α) as the frequency at which viral strains acquire genetic changes. At each time step, a viral strain mutate into another strain with the mutation rate α. This parameter, set to 10^{-2}, captures the evolutionary dynamics of the virus, reflecting its ability to adapt and evolve over time.

Furthermore, the possible states of a node in our model are clearly defined. Each individual may be in exactly one of the following states at any given time:

- S: A susceptible individual (can become infected).
- I_j: An infected individual with strain j (can transmit the infection to susceptible individuals).
- R_j: A recovered individual from strain j (immune to strain j but may be susceptible to other strains).

Here, $j = 1, \ldots, k$, where k represents the total number of strains in the system. This system of states ensures that the model tracks the progression of each individual through different infection states, with potential for mutation to other strains over time.

These parameter choices align with realistic scenarios encountered in the epidemiology of respiratory infections, providing a meaningful framework for studying disease dynamics. Notably, under these parameter settings, the basic reproduction number exceeds one for the analyzed examples, indicating the potential for sustained transmission within the population. This metric serves as a critical determinant of epidemic potential and informs public health interventions aimed at disease control and prevention.

As evidenced in Figs. 4.3 and 4.4, which present the above scenarios in the two networks through multiple simulations implemented via the Gillespie algorithm (see Pseudocode Algorithm 1 where it has been sketched for a simple SIR model with a single strain and no mutation), the dynamics of disease spread vary significantly between these network models.

In the RSG network model (depicted in panel (b) of both figures), nodes are arranged based on their physical proximity, with edges representing spatial connections rather than preferential attachment according to node degree. This spatial arrangement results in nodes that are physically close to each other being more likely to be connected by edges, reflecting the underlying geography or spatial distribution of the nodes. Consequently, the network exhibits a more homogeneous distribution of connections compared to networks generated by preferential attachment mechanisms like the Barabási–Albert model.

This uniform connectivity pattern in the RSG network leads to a lack of highly connected hubs or nodes with exceptionally high degrees. In contrast, the SF model (panel (a)) forms hubs through preferential attachment, resulting in highly connected nodes that act as hotspots for disease transmission. These hubs facilitate rapid disease propagation by enabling infections to spread efficiently through densely connected regions of the network.

As a result, disease transmission within the RSG network, despite possessing an equal number of connections (edges) to the SF network, exhibits lower efficiency. Infections progress more gradually through the RSG network due to the lack of highly connected hubs, which typically serve as primary pathways for transmission. In contrast to the SF network, where rapid transmission occurs via these hubs, in the RSG network, infection spread is constrained by the spatial proximity of nodes and the density of connections within their immediate surroundings. To ensure the reliability and consistency of our results, each simulation scenario was repeated multiple times. In all iterations, the network structure—whether SF or RSG—was kept fixed, maintaining consistent node connectivity and topology. Furthermore, each iteration was initialized identically, with node 1 infected by the first strain, providing a uniform baseline for evaluating the effects of network topology and mutation dynamics on disease spread.

(a) *(b)*

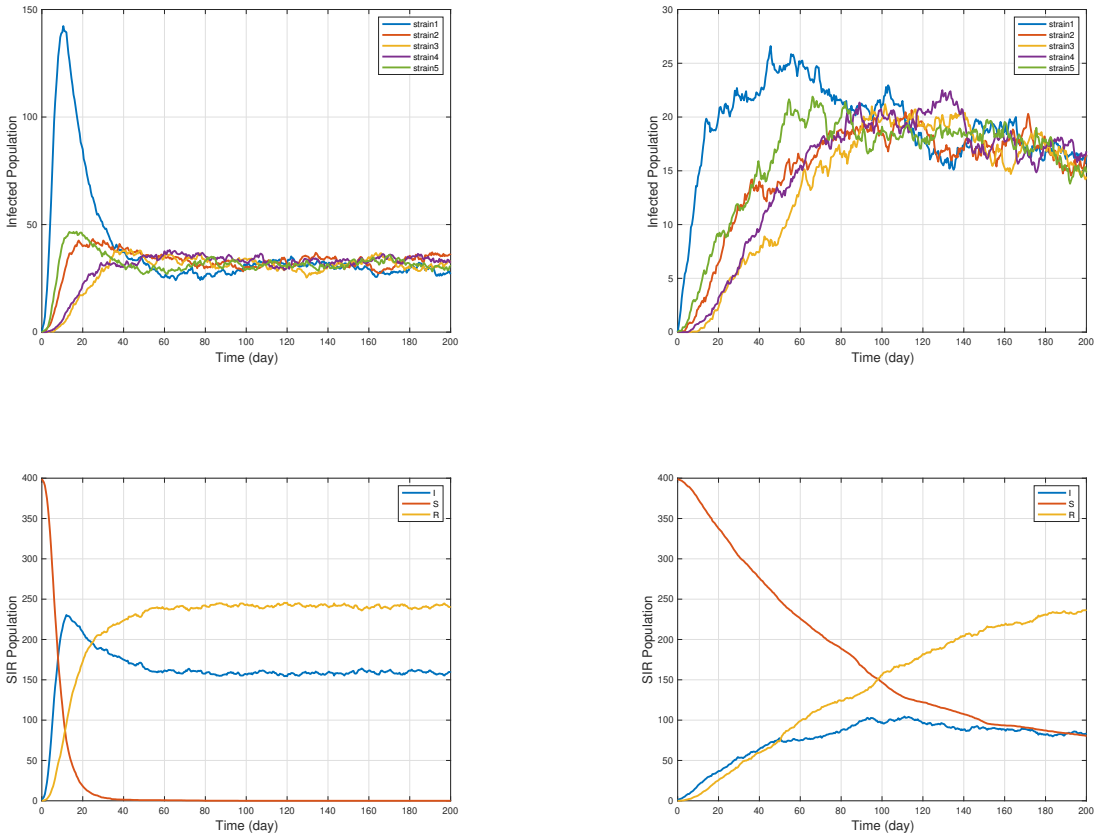

Figure 4.3: *Scenario* 1 *Analysis: This figure presents a comparison of epidemic spread dynamics across scale-free networks in panel (a) and random spatial-geometric network in panel (b), with* $N = 400$ *and 100 simulations using the Gillespie algorithm, where strains can mutate to either the preceding or following strain, and recovery does not guarantee immunity against other variants. Despite both networks having an equal number of connections (edges), the spatial network exhibits slower infection spread due to the absence of highly connected hubs, which act as primary pathways for transmission in the SF network. In the spatial network, infection spread is constrained by the spatial proximity of nodes and the density of connections within their immediate surroundings.*

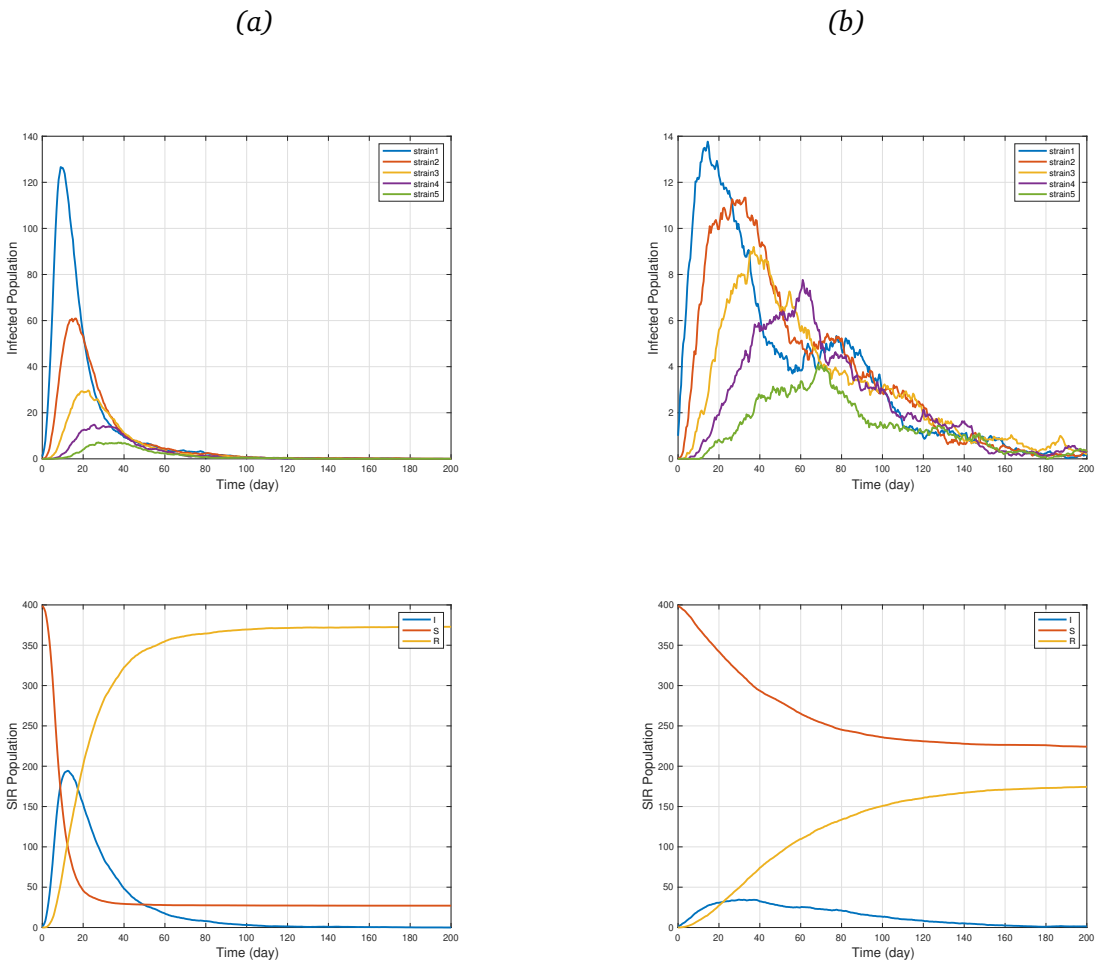

Figure 4.4: *Scenario 2 Analysis: Comparison of epidemic spread dynamics between Scale-Free networks (panel a) and Random Spatial-Geometric networks (panel b) with N=400 nodes and 100 simulations using the Gillespie algorithm. Under conditions where strains mutate sequentially and recovery only provides immunity against previous strains, the spatial network demonstrates slower infection spread despite possessing an equal number of connections (edges) to the SF network. This difference can be attributed to the absence of highly connected hubs in the spatial network, which serve as primary pathways for transmission in the SF network. In the spatial network, infection spread is constrained by the spatial proximity of nodes and the density of connections within their immediate surroundings.*

4.3.1 Control Strategies for Disease Spread

In this section, we aim to control the spread of disease by employing global social distancing strategy (SDS). Control measures, including this strategy, reflect a concerted effort to suppress or at least slow down the spread of the virus. Social distancing minimizes opportunities for virus transmission by maintaining physical distance between individuals and reducing the frequency of gatherings in large groups. [8].

Various social distancing measures have been implemented in response to the COVID-19 pandemic. These measures include the closure of schools, workplaces, and certain businesses, as well as the cancellation of events to prevent large gatherings. In some countries, initial measures involved the prohibition of mass gatherings exceeding 1000 people. However, as the situation evolved, this limit was progressively reduced to 500 and then further down to 50 individuals. Additionally, cinemas, restaurants, gyms, and places of worship were closed in some regions. Germany, for instance, opted to close most non-essential shops while extending the operating hours of supermarkets. This adjustment aimed to minimize crowding by spreading out customer visits. Furthermore, certain countries implemented special measures to protect vulnerable populations, such as reserving the first hours of business for elderly customers who are at higher risk of severe illness [24].

While social distancing as a non-pharmaceutical intervention has been incorporated into network-based epidemic models in several studies [50, 61], this section distinguishes itself by implementing social distancing within the two specific scenarios proposed in this work.

We analyze the impact of this intervention by modeling a global social distancing strategy. In this strategy, social distancing is activated when the virus prevalence—that is, the proportion of infected individuals in the population—reaches a predetermined threshold. Once this threshold is crossed, all individuals in the population are required to reduce their contacts, regardless of their infection status. In the network model, this is implemented by randomly removing a fraction σ_G of all edges, including connections between any combinations of individuals.

The timing of this intervention—that is, when social distancing is actually triggered—is shown by a vertical dashed line. Each figure shows the average result from several simulation runs. In some of these runs, the total number of infected individuals never reaches the threshold, because the outbreak fades out due to recovery. In such cases, social distancing is not applied at all. As a result, the average number of infected individuals under social distancing conditions might appear lower than the threshold, even though the intervention is meant to begin when that threshold is crossed.

It is also important to note that the dashed line in the figures represents the average time at which social distancing is applied across all simulations. In some runs, the threshold is reached quickly, while in others it takes longer. When we average the timing across all these cases, the dashed line may end up appearing after the peak of the outbreak. This can give the impression that social distancing was applied too late. However, in the runs where the threshold was actually reached, the intervention was applied promptly.

In our model, social distancing is simulated by randomly removing network connections by a specified percentage, which is adjustable. This method allows us to explore the effects of varying intensities of non-pharmaceutical interventions on the spread of the virus. By adjusting the extent to which these connections are cut, we can assess the effectiveness of different levels of intervention rigor. This approach provides valuable insights into how varying degrees of social distancing can influence the dynamics of disease transmission and inform optimal public health strategies. For example, in very large population countries such as India and Brazil, adopting stricter social distancing measures will play a crucial role in preventing the overwhelming of healthcare services and averting thousands of deaths due to inadequate care for severe cases of the disease [8]. We present three distinct degrees of social distancing: no social distancing ($\sigma_G = 0$), the results shown in the previous section; a moderate degree of SD ($\sigma_G = 0.4$); and a high degree of SD ($\sigma_G = 0.7$).

Similarly to the previous subsection, we implement the simulations for two different random graphs: Scale-Free network and Random Spatial-Geometric network.

4.3.1.1 Global Social Distancing

We first examine the impact of a moderate degree of global social distancing ($\sigma_G = 0.4$) on our two scenarios, comparing it with the results observed in the previous section where no social distancing measures were in place. Initially, we use a 'null network' configuration, which represents the societal state before any stringent global distancing measures were introduced [12, 43]. This baseline scenario allows us to observe the natural progression of the disease without interventions. Once the number of infected individuals reaches 5% of the total population, we implement global social distancing. This intervention transitions the simulation to a network where connections per agent are significantly reduced, representing a moderately reduced interaction model.

The implementation of this control strategy yielded distinct outcomes across the two scenarios and network topologies. Figs. 4.5 and 4.6 illustrate these effects, highlighting the nuanced interplay between social distancing, network structure, and the characteristics of viral mutation and immunity in each scenario.

In the second scenario (Fig. 4.6), characterized by sequential viral mutation and cumulative immunity, the introduction of global social distancing significantly altered disease transmission dynamics. The reduction in global contacts among individuals led to a noticeable decrease in the infection levels across the network. Compared to the baseline scenario without interventions (Fig. 4.4), the infected population was reduced by more than 70% when social distancing was applied. This pronounced effect reflects the way in which intervention strategies interact with the structure of viral mutation and host immunity.

One possible explanation for this is that, in this scenario, the emergence of new viral strains occurs sequentially through mutation, with individuals infected by earlier strains gaining immunity to later strains. As a result, the epidemic trajectory is tightly coupled to the success of early strains in establishing transmission chains. Social distancing not only reduces the initial strain direct spread but also indirectly

preventing or delaying the appearance of subsequent variants. Furthermore, due to the one-way cross-immunity, individuals exposed to the primary strain become protected against the secondary strain, narrowing the susceptible population available for future transmission. This combination of slowed primary transmission and immunological shielding amplifies the overall effect of social distancing.

In the first scenario (Fig. 4.5), which involves dynamic viral mutation and partial cross-immunity patterns, also exhibited a substantial decline in infection levels under global social distancing (compare with Fig. 4.3). However, the relative reduction was smaller than in the second scenario. In this setting, strains can evolve and circulate independently, and the absence of cross-immunity allows for repeated infections across different strains. As a result, while social distancing still reduces contact rates and slows transmission across the network, it does not disrupt any directional dependency or protection between strains. Each strain retains access to a largely unaffected susceptible population, making the intervention less efficient in limiting cumulative infections.

These results highlight how the interaction between viral mutation dynamics and host immunity influences the effectiveness of non-pharmaceutical interventions. In scenarios with constrained mutation pathways and cumulative immunity, social distancing has amplified effects by disrupting not just immediate transmission but also the conditions for future strain emergence. Conversely, when strains are immunologically and evolutionarily independent, interventions must work harder to suppress each wave individually. This insight supports tailoring control strategies to the underlying viral dynamics and host immune interactions.

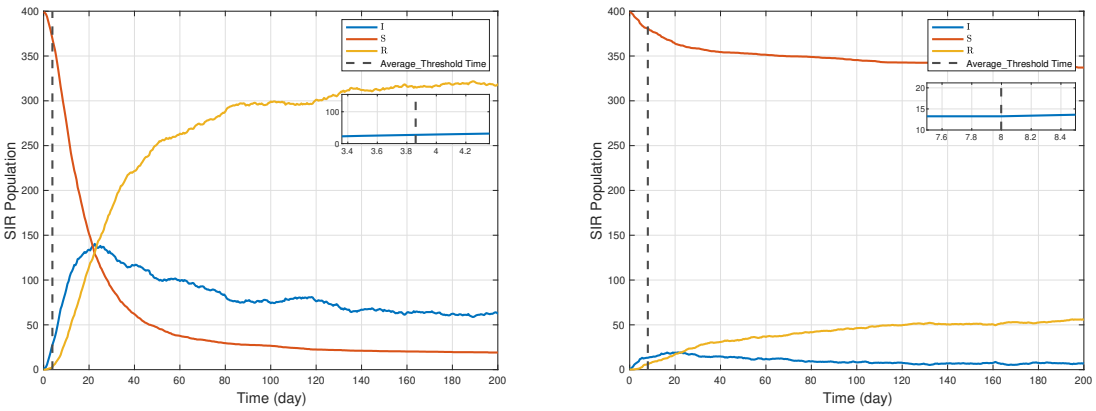

Figure 4.5: *Implementation of global social distancing in Scenario 1 on SF and RSG networks, depicted in panels (a) and (b) respectively, with a population size of* $N = 400$ *and 100 simulations. Upon reaching a threshold where the total infected population constitutes 5% of the entire population (dashed line), a moderate social distancing strategy is initiated, involving the removal of 40% of all connections.*

In Figs. 4.7 and 4.8, we analyze the total infected populations across three levels of social distancing intensity: no social distancing, moderate social distancing

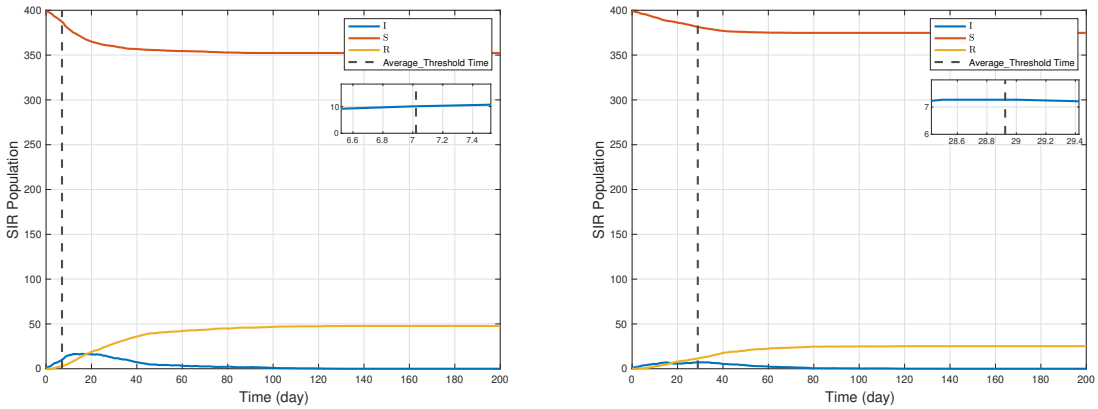

Figure 4.6: *Implementation of global social distancing in Scenario 2 on SF and RSG networks, in panels (a) and (b) respectively. The population size is $N = 400$. Once the total infected population reaches 5% of the entire population (dashed line), a moderate social distancing strategy is enacted, entailing the removal of 40% of all connections.*

($\sigma_G = 0.4$), and high social distancing ($\sigma_G = 0.7$). The results reveal a clear gradient in infection outcomes, with progressively lower infected populations as the intensity of social distancing increases. This trend underscores the critical role of intervention measures in mitigating disease spread and their effectiveness across different network structures.

No Social Distancing: In the absence of any social distancing measures, the infected population remains consistently high across both the SF and RSG networks. This case reflects the rapid and uncontrolled spread of the virus, particularly in environments lacking intervention. The SF network, with its highly connected hubs, facilitates efficient transmission, making it especially vulnerable to widespread outbreaks under these conditions. Similarly, the RSG network, while less efficient in spreading the virus due to its spatial constraints, still experiences significant infection levels when no control measures are implemented. The simulations with no social distancing are shown in previous section in Figs. 4.3 and 4.4.

Moderate Social Distancing ($\sigma_G = 0.4$): The introduction of moderate social distancing has a substantial impact on disease dynamics. In both networks (Figs. 4.7 and 4.8), moderate social distancing effectively reduced the infected population compared to the no-intervention scenario. By targeting and reducing connections, this intervention significantly disrupts transmission pathways, curbing the virus's ability to propagate. In the RSG network in particular, the impact of moderate social distancing is more pronounced.

High Social Distancing ($\sigma_G = 0.7$): High social distancing measures result in a dramatic reduction in the infected population, especially in the SF network. By removing a substantial fraction of connections, this intervention nearly eliminates the influence of highly connected hubs, effectively severing the primary pathways for viral transmission. As shown in panel (a) of Figs. 4.7 and 4.8, this level of intervention

disrupts the transmission chain so thoroughly that it leads to a precipitous drop in infections, demonstrating the unparalleled efficacy of stringent measures in scale-free networks.

However, in the RSG network (panel (b) of Figs. 4.7 and 4.8), the difference between moderate and high social distancing is relatively minor. Nevertheless, it is evident that implementing a high degree of social distancing leads to the extinction of the infected population significantly earlier compared to the moderate degree. Due to the uniform distribution of connections and the absence of highly influential nodes, increasing the intensity of social distancing beyond a certain threshold yields diminishing returns. The infection levels remain lower than in the no-intervention scenario, but the relative gain between moderate and high distancing is less significant than in the SF network.

The differing responses of the SF and RSG networks to varying levels of social distancing highlight the importance of network topology in determining the effectiveness of intervention strategies. The SF network, characterized by its hubs, exhibits a clear benefit from increasing the intensity of social distancing. Disrupting the hubs has a disproportionate impact, as these nodes are responsible for the majority of transmissions. On the other hand, the RSG network, with its homogeneous connectivity and reliance on spatial proximity, demonstrates a more uniform response to interventions. Once a certain level of distancing is achieved, further reductions in connectivity do not significantly enhance control efforts.

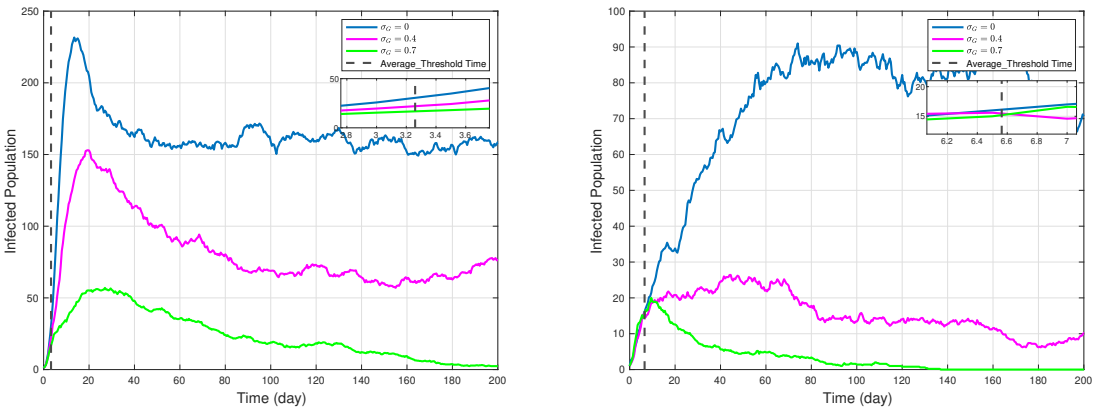

Figure 4.7: *Comparison of total infected populations under varying degrees of global social distancing in SF and RSG networks in Scenario 1, depicted in panels (a) and (b) respectively. The simulations were conducted with a total population size of $N = 400$, where global social distancing measures were implemented once 5% of the population was infected (dashed line). Three degrees of social distancing were examined: no social distancing ($\sigma_G = 0$), moderate social distancing ($\sigma_G = 0.4$), and high social distancing ($\sigma_G = 0.7$). Each simulation was run for 50 iterations to observe the effects on the total infected populations.*

These findings emphasize the necessity of tailoring social distancing policies to

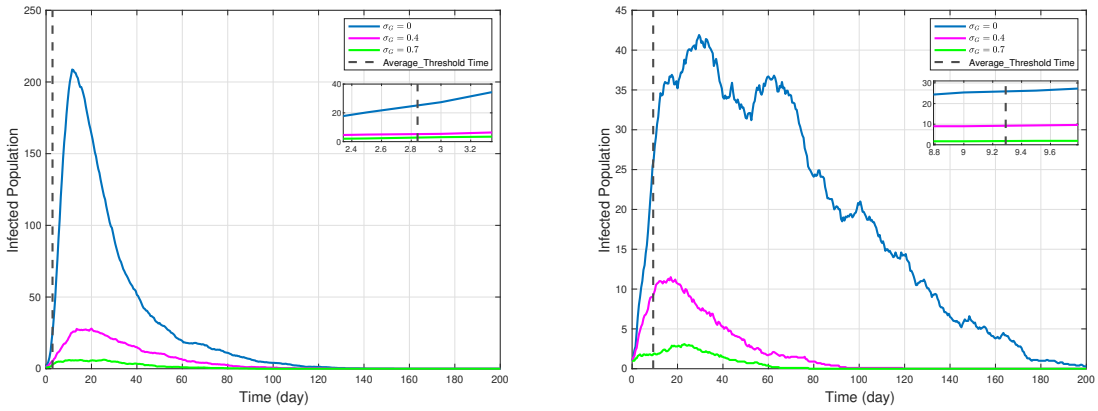

Figure 4.8: *Total infected populations under varying degrees of global social distancing in (a) SF and (b) RSG networks for Scenario 2. Simulations were performed with a population size of $N = 400$, where global social distancing measures were initiated once 5% of the population became infected (dashed line). Three levels of social distancing were analyzed: no social distancing ($\sigma_G = 0$), moderate social distancing ($\sigma_G = 0.4$), and high social distancing ($\sigma_G = 0.7$). Each simulation ran for 50 iterations to assess the impact on the total infected population size.*

the underlying network structure of a population. In environments resembling SF networks, where a few individuals or locations serve as major transmission hubs, high-intensity social distancing can be an exceptionally effective strategy for controlling outbreaks. Although, moderate social distancing is still impactful. Conversely, in settings similar to RSG networks, where connectivity is more evenly distributed, moderate social distancing may suffice to achieve substantial reductions in infection levels, minimizing the need for overly restrictive measures.

This analysis reinforces the critical role of social distancing as a non-pharmaceutical intervention, especially during epidemic peaks. By adapting the intensity of distancing measures to the specific characteristics of the population's interaction network, public health officials can maximize the effectiveness of these interventions while minimizing societal disruption.

The strategic timing of implementing social distancing measures is pivotal in the effective management of infectious disease outbreaks. Initiating these interventions right after the onset of an outbreak can significantly influence their efficacy. This principle is supported by our simulations presented in Figs. 4.9–4.10, which are conducted across the two networks in Scenarios 1 and 2, and highlight the critical importance of timely action. The results specifically illustrate that implementing social distancing measures when only 2.5% of the population (i.e., 10 individuals) is infected, as opposed to waiting until 5% or 10% are infected, can significantly accelerate the control of the disease outbreak.

Our comparative analysis underscores a notable divergence in infection dynamics between the SF and RSG networks when social distancing measures are imple-

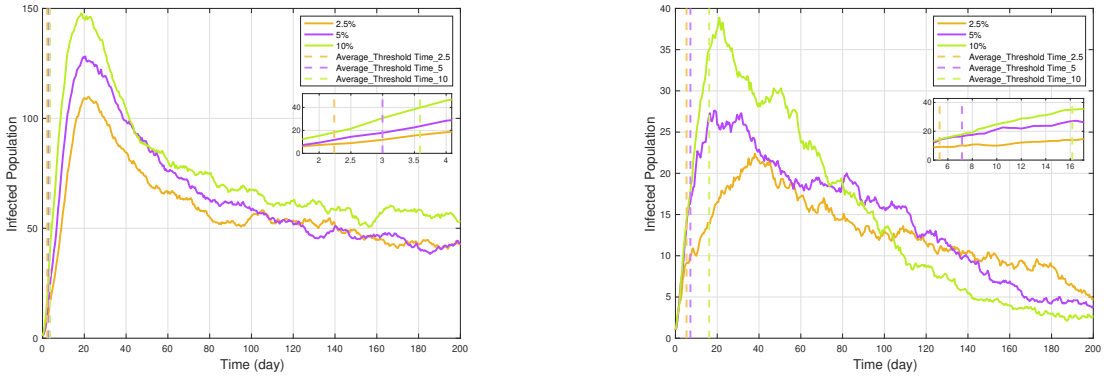

(a) *Moderate distancing ($\sigma_G = 0.4$).*

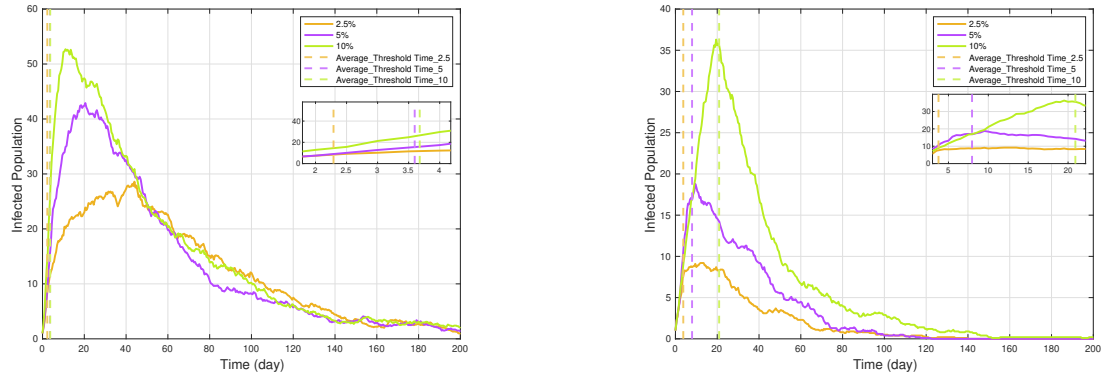

(b) *High distancing ($\sigma_G = 0.7$).*

Figure 4.9: *Analysis of global social distancing timing in SF and RSG networks (left and right panels, respectively) under Scenario 1 with (a) moderate social distancing ($\sigma_G = 0.4$) and (b) high social distancing ($\sigma_G = 0.7$). Simulations were conducted with $N = 400$ nodes and 50 iterations. Early interventions (2.5% infected) significantly reduce epidemic peaks in both networks compared to delays at 5% and 10% infected.*

mented. Specifically, in the RSG network (panel (b) of Figs. 4.9–4.10 corresponding to both Scenario 1 and Scenario 2), as well as in the SF network under Scenario 1, delays in enforcing social distancing lead to higher infection peaks and prolong the duration of the virus within the community. Thus, the precision in timing these interventions is critical for minimizing both the peak and the duration of an epidemic in these networks.

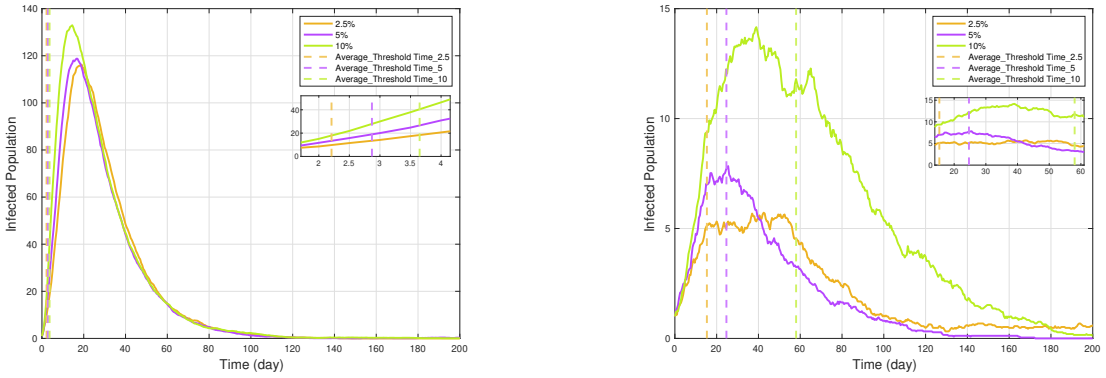

(a) *Moderate distancing ($\sigma_G = 0.4$).*

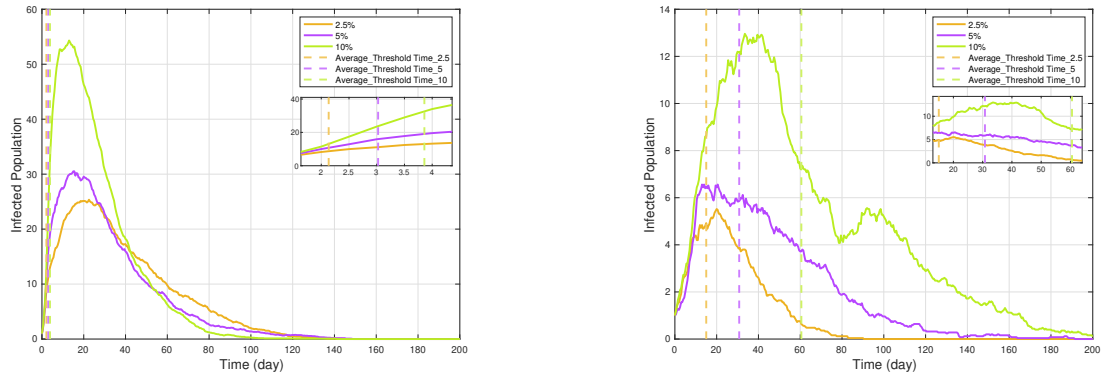

(b) *High distancing ($\sigma_G = 0.7$).*

Figure 4.10: *Analysis of global social distancing timing in SF and RSG networks (left and right panels, respectively) under Scenario 2 with (a) moderate social distancing ($\sigma_G = 0.4$) and (b) high social distancing ($\sigma_G = 0.7$). Simulations were conducted with $N = 400$ nodes and 50 iterations. (a) In the SF network, the epidemic trajectory is largely unaffected by intervention timing, while delayed interventions in the RSG network lead to higher peaks and longer outbreaks. (b) Early interventions (2.5% infected) significantly reduce epidemic peaks in both networks compared to delays at 5% and 10% infected under higher degree.*

Our simulations on the SF network under Scenario 2 reveal that when a moderate degree of social distancing is applied (left panel of Figs. 4.9(a) and 4.10(a)),

the timing of these interventions—whether at 2.5%, 5%, or 10% of the population infected—does not significantly change the epidemic's trajectory. However, this changes markedly with the application of more stringent social distancing measures (see Fig. 4.9(b) and Fig. 4.10(b)). Under highly intensive interventions, the timing of implementation becomes crucial. Specifically, initiating strict social distancing earlier in the epidemic's course—such as when only 2.5% of the population is infected—can significantly reduce the peak of the epidemic. This indicates that while moderate social distancing may be ineffective in altering the spread in highly interconnected networks like the SF under Scenario 2, the strategic timing of more severe measures can mitigate the epidemic's impact.

The difference in the impact of timing social distancing measures between cases with different levels of edge removal (moderate and high) can be attributed to how effectively the interventions disrupt transmission pathways in the SF network, particularly in the presence of highly connected hubs. Therefore, even when social distancing measures are implemented relatively early in the outbreak (say 2.5% of the population is infected), the remaining network structure still facilitates considerable transmission, leading to a relatively modest decrease in the outbreak peak compared to when social distancing is implemented later (when 10% of the population is infected).

However, in the case with a 0.7 fraction of edge removal (high degree), a larger proportion of the network's edges are removed, including many of the highly connected hubs. As a result, the network becomes more disconnected, with fewer ways for the disease to spread. When social distancing measures are implemented early in the outbreak, the reduced connectivity of the network limits the spread of the virus more effectively, resulting in a lower outbreak peak. Conversely, when social distancing measures are implemented later, the virus has already spread extensively through the network, and the remaining connectivity still allows for significant transmission, leading to a higher outbreak peak compared to the earlier implementation.

The reason why the timing of social distancing appears less impactful under Scenario 2 compared to Scenario 1 is likely due to the way infections initially spread in the network. In Scenario 2, the early infections tend to remain more localized within smaller clusters rather than spreading quickly throughout the entire network. As a result, the outbreak grows more slowly at the beginning, which reduces the urgency and effectiveness of early intervention—especially when moderate social distancing is applied. This means that whether social distancing starts when 2.5% or 10% of the population is infected makes less of a difference to the overall outcome. However, when stronger social distancing measures are used—particularly those that remove a large number of connections including key hubs—the timing becomes much more important. In these cases, acting early helps cut off major transmission routes before the virus spreads widely, significantly lowering the outbreak peak.

5 Evolution into chaos – implications of the trade-off between transmissibility and immune evasion

Predicting the evolution of viruses is both a significant challenge and a major public health concern. Numerous studies have investigated virus evolution by introducing a trade-off between pathogens' epidemiological traits (virulence, transmissibility, and clearance). However, the majority of these investigations have primarily focused on the trade-off between virulence and the transmissibility. Anderson and May [9] argued that a parasite cannot increase its transmission rate without shortening its infectious period by harming its host, and they showed that the parasite should adopt an optimum intermediate level of virulence. This trade-off approach inspired many subsequent works. This phenomenon is explored in detail in Chapter 11 of the book "Evolutionary Dynamics" [64], where the epidemiological dynamics of at least two parasite strains competing for the same host have been studied. If transmissibility is proportional to virulence, the basic reproduction number is an increasing function of virulence, and selection favors strains with higher virulence and thus higher infectivity. However, when transmissibility is a saturating non-linear function of virulence, the basic reproduction number becomes a hump-shaped function of virulence, maximized at an optimal intermediate level. Therefore, if the virulence of a parasite population is greater than this value, then selection will reduce virulence; otherwise, it will increase it.

The study [2] investigated the emergence of a convex trade-off between transmission and virulence, utilizing a model that explicitly incorporates within-host dynamics. Their analysis indicated the robustness of this convex trade-off. Additionally, they demonstrated that small variations among parasites or hosts might blur the trade-off curve, as parasites with the same within-host growth rate can express different virulence or transmission values for each host they infect. Further in-depth discussion of the transmission–virulence trade-off can be found in [1, 3, 57, 68] and references thereof.

Other models have been developed that incorporate trade-offs between additional traits. For instance, [47] modeled an inherent trade-off between contact and transmissibility using a basic susceptible–infected–recovered (SIR) framework by differentiating between mild and severe infections to indicate that increasing symptom

severity will tend to decrease contact rates and increase the probability of transmission given contact. The work [79] studied the host-pathogen interaction for the case in which hosts may become at most doubly infected. It was discovered that in the presence of frequent double infections, increased virulence is favored; but when pathogens become more virulent, the force of infection will decrease, followed by lower virulence again. They concluded that the endemic steady state of the virulence depends on the interaction within hosts as well as on the interaction at the population level.

On 12 March 2020, the World Health Organization (WHO) declared a new worldwide pandemic, COVID-19, which originated in China in December 2019 and rapidly spread around the world, causing millions of deaths [60]. The most common SARS-CoV-2 variants of concern, including the wild type, Alpha, Beta, Gamma, Delta, and Omicron, show great diversity in their transmissibility and virulence [40, 45, 59].

This diversity, and the need to assess the evolutionary trajectory of new variants, urged scientists to re-examine the potential trade-off between virulence and transmissibility of SARS-CoV-2 [44]. Other studies of SARS-CoV-2 evolution explore how different vaccination strategies could impact infection dynamics and antigenic evolution in partially immune populations [72], or discuss the impacts of immune escape and transmissibility on the endemic load of SARS-CoV-2 [65]. A major concern related to new variants was their ability to evade immunity and its potential impact on the severity of upcoming waves [16, 73, 78]. According to [21], antibody resistance may compromise viral fitness, such as in the B.1.351 variant, which resists neutralization by antibodies but also loses enhanced transmissibility as a consequence of the immune-escape mutations. The JN.1 variant showed higher immune evasion compared with BA.2.86 and other strains, at the expense of reduced human ACE2 binding, and this evolutionary pattern has been observed in the previous transition from BA.2.75 to XBB [86]. Hence, it is natural to consider a potential trade-off between immune evasion and transmissibility. Such a trade-off is further supported by the analysis published in [67].

While the classical trade-offs have been extensively investigated, there remains a significant gap in the mathematical understanding of the implications of a trade-off between transmissibility and immune evasion. Viral evolution often operates under selective pressures that favor maximizing the basic reproduction number $\mathcal{R}_0$, which measures the average number of secondary infections caused by a single infected individual in a fully susceptible population. In our framework, however, optimal evolutionary strategy depends on the resident strain, and refers to the evolutionary pathway that maximizes the invasion fitness of a viral strain balancing the trade-off between immune evasion and transmissibility. Understanding this balance is crucial for predicting the long-term behavior of pathogens and developing effective public health interventions.

To account for such a trade-off in viral evolution, we construct a novel evolutionary model by the following steps (Fig. 5.1):

1. We initiate our analysis by investigating an SIR system with a single strain in an endemic steady state.

2. Upon the emergence of new strains distinct from the previous strain, we introduce a parameter $p \in [0, 1]$ to denote their immune-evasive property, which represents the fraction of recovered individuals from the resident strain that can be infected by the new strain. Strains with $p = 0$ are unable to infect anyone with prior immunity, while strains with $p = 1$ can infect all individuals. Additionally, we assume a trade-off between transmissibility and immune evasion, making the transmission rate of new strains dependent on p. Subsequently, our focus shifts to the introduction of novel strains, aiming to ascertain whether their emergence is attributed to their ability to evade immunity or their heightened transmissibility.

3. Next we select the fittest strain by maximizing the invasion fitness, and the system goes to the new endemic steady state characterized by this new strain with a new transmission rate determined by the trade-off function.

4. Return to step 1 and continue the evolutionary process.

This evolutionary process is depicted in Fig. 5.1. Although many adaptive dynamics frameworks emphasize the role of small mutational steps in evolutionary processes [17], our model distinguishes itself by allowing larger evolutionary jumps with significant differences between resident and invader strains. This reflects real-world observations such as the COVID-19 pandemic, where, from a given host population's perspective, the evolution was characterized by the emergence of vastly different strains with the ability of replacing the resident strain without a gradual sequence of mutations (which may have occurred elsewhere). An important aspect of our model is the difference between the epidemiological dynamics of the resident and invader strains. Specifically, the resident strain cannot infect recovered individuals due to acquired immunity. In contrast, invader strains may exhibit varying degrees of immune evasion, which allows them to re-infect a part of the recovered population. This asymmetry is important to shape the invasion fitness of new strains and influences the direction of their evolutionary trajectory.

Through our theoretical framework, we shall investigate whether in the short term such evolution points towards enhanced transmissibility or enhanced immune evasion (Theorem 5.1.1). We analyze the transmissibility and the immune evasion capability of successive invading strains, and explore this evolution over the long term as well. We provide explicit conditions when the evolution converges to a certain transmissibility (Theorem 5.2.2), but we also find situations when there exists an alternating pattern of period two where highly transmissible and immune evasive strains repeat (Theorem 5.2.8). The most interesting case is when the evolution exhibits chaotic behaviour, thus making viral evolution unpredictable (Theorem 5.2.13). Our findings are illustrated by corresponding figures, charts and the bifurcation diagram (see Figs. 5.4–5.6).

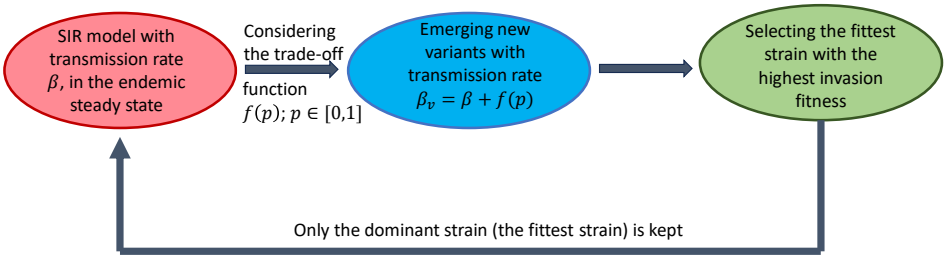

Figure 5.1: *The model outline flowchart: Beginning with the SIR model with a transmission rate β, while the system is in an endemic steady state (red). New strains with immune-evasive property p, where $p \in [0,1]$, emerge. Assuming a trade-off between transmissibility and immune evasion, denoted by $f(p)$, the transmission rates of these new strains are $\beta_v = \beta + f(p)$ (blue). As the evolution tends to favor the strain with maximal invasion fitness (maximizing the invasion reproduction number), we consider the newly emerging strain which is the fittest with a transmission rate $\beta_v = \beta + f(p^{\max})$ (green). The system transitions to a new endemic steady state characterized by a novel transmission rate determined by the trade-off function. The process returns to the initial step and the evolutionary process is continued.*

5.1 Direction of the viral evolution: higher transmissibility or immune evasion?

In this section, we aim to ascertain the direction of the virus's evolution. We seek to identify the circumstances under which the virus's evolutionary path inclines toward heightened transmissibility or increased immune evasion. Additionally, we investigate the conditions under which a newly emerging strain can successfully invade the resident strain.

Consider the SIR Model (2.1) from Chapter 2. We introduce invader strains, denoted by the index v into the system, we aim to discern whether the emergence of this invader strain is attributable to its capacity to evade immunity or its enhanced transmissibility. This introduction is made under the assumption that the system attains its endemic steady state:

$$(S^*, I^*, R^*) = \left(\frac{1}{\mathcal{R}_0}, \frac{\mu}{\beta}(\mathcal{R}_0 - 1), \frac{\gamma}{\beta}(\mathcal{R}_0 - 1)\right), \tag{5.1}$$

where the basic reproduction number $\mathcal{R}_0 = \frac{\beta}{\gamma+\mu} > 1$ ensures that the endemic steady state exists and is globally attractive.

In contrast to the slow mutation process inherent in many evolutionary models, our model distinguishes itself by allowing for the invasion of strains by a diverse array of variants, rather than solely mutants of the resident strain with very similar parameters. Many populations experienced such situation during COVID-19, where the evolution progressed to many different directions in other parts of the world, and

countries were facing a large number of new strains originated from elsewhere, and some of those were able to invade and replace the previously dominant strain. These newly emerging strains, referred to as invader strains, differ from the resident strain in two distinct ways:

- Immune Evasion: Invader strains have the capability to evade immunity and infect individuals who have recovered from the resident strain (R). To quantify this, we introduce the parameter $p \in [0, 1]$ which represents the fraction of recovered individuals from the resident strain that can be infected by the new strain.
- Transmissibility: Invader strains may exhibit either heightened or diminished contagiousness relative to the resident strain. This is delineated by the parameter $\beta_v = \beta + f(p)$, where $f(p)$ represents the trade-off function between transmissibility and immune evasion. A positive value of $f(p)$ indicates an enhanced transmissibility of the invader strain compared to the resident strain, while a negative $f(p)$ suggests a reduction in transmissibility. This trade-off function operates under the following assumptions:

(H1) f is continuously differentiable on $[0, 1]$;

(H2) $f'(p) < 0$, for $p \in [0, 1]$;

(H3) $f(0) > 0$ and $f(1) < 0$.

The early dynamics associated with the invader strain, represented by linearization at the endemic equilibrium, and characterized by the transmission rate β_v, can be expressed as follows:

$$\dot{I}_v(t) = \beta_v S^* I_v(t) + \beta_v p R^* I_v(t) - \gamma I_v(t) - \mu I_v(t). \tag{5.2}$$

Therefore, the invasion reproduction number for the invader strains when the resident strain is in its endemic steady state, is

$$\mathcal{R} = \frac{(\beta + f(p))(S^* + pR^*)}{\gamma + \mu} = \frac{\beta + f(p)}{\gamma + \mu}\left[\frac{(\mu + \gamma)}{\beta} + \frac{p\gamma(\beta - (\mu + \gamma))}{\beta(\mu + \gamma)}\right], \tag{5.3}$$

which denotes the number of secondary infections produced by an individual infected with the invasive variant over the course of their infectious period, within a population where resident strains have achieved equilibrium [58]. This can be interpreted as follows: An infectious individual remains infectious for $1/(\mu + \gamma)$ time units. The number of new infections produced by a single infected host is given by $(\beta + f(p))(S^* + pR^*)$ per unit time, since the available pool for infection with immune evasion parameter p is $S^* + pR^*$. The product of these two quantities is the number of secondary infected cases that are caused by one infection. The equilibrium abundance of uninfected hosts prior to the arrival of the infection compartment by

invader strains is given by (5.1). Hence (5.3) represents the invasion reproductive ratio, which is a crucial quantity that determines whether a virus can spread in a host population. If $\mathcal{R} < 1$, the population infected by the invader is expected to diminish over time, whereas, $\mathcal{R} > 1$ measures the potential for the novel strain to continue spreading and potentially invade the population.

In the subsequent theorem, we will show that when β is small, the invasion reproduction number is a monotone decreasing function of p, indicating the emergence of a new strain with a higher transmission rate. Conversely, in case of high transmission rate β, circumventing the immune system is the most advantageous evolutionary strategy for the invader strain.

Theorem 5.1.1. *Let f satisfy (H1)–(H3). We assume the resident strain of Model* (2.1) *is in its endemic steady state, as given by* (5.1). *Then, there exists sufficiently small $\delta > 0$ such that if $\beta \in (\mu + \gamma, \mu + \gamma + \delta)$, then the invasion reproduction number $\mathcal{R}(p)$ decreases on $[0, 1]$, and it attains its maximum at $p = 0$ and $\beta_v = \beta + f(0)$. For large values of β, $\mathcal{R}$ is an increasing function of p on $[0, 1]$, hence the maximum of $\mathcal{R}(p)$ occurs at $p = 1$ and $\beta_v = \beta + f(1)$.*

Proof. To prove the theorem, it is enough to show that for small β, $\mathcal{R}'(p)$ is negative, and for large β, $\mathcal{R}'(p)$ is positive on $[0, 1]$ (here $'$ denotes the derivative with respect to p).

Straightforward calculation yields

$$\mathcal{R}'(p) = \frac{\gamma(\beta - (\mu+\gamma))(\beta + f(p)) + ((\mu+\gamma)^2 + p\gamma(\beta - (\mu+\gamma)))f'(p)}{\beta(\mu+\gamma)^2} \tag{5.4}$$

$$= \frac{\gamma}{(\mu+\gamma)^2}\beta + \frac{(f(p) + pf'(p) - (\mu+\gamma))\gamma}{(\mu+\gamma)^2} + \frac{f'(p)((\mu+\gamma)^2 - p\gamma(\mu+\gamma)) - \gamma f(p)(\mu+\gamma)}{\beta(\mu+\gamma)^2}. \tag{5.5}$$

Since $f \in C^1[0, 1]$, there exist positive constants k and K such that $|f(p)| < K$ and $-K \leq f'(p) \leq -k$ hold for all $p \in [0, 1]$. Combining this with (5.4), it follows that if $\beta - (\gamma + \mu)$ is sufficiently small, then $\mathcal{R}'(p) < 0$ holds for all $p \in [0, 1]$, since with $\beta \to \mu + \gamma$ we are left with $f'(p)/\beta < -k/\beta < 0$. This implies that the function $\mathcal{R}$ is decreasing throughout and the maximum of $\mathcal{R}$ occurs at $p = 0$.

On the other hand, considering the boundedness of both f and f', we observe that for sufficiently large β, the first term dominates in (5.5), hence $\mathcal{R}'(p)$ is positive for all $p \in [0, 1]$ and it attains its maximum at 1. □

The result of this theorem is intuitive: if the reproduction number is very large, then the recovered population at the steady state is also large, hence immune evasion can be very beneficial for a new strain. However, it does not gain much from immune evasion when the reproduction number is only slightly larger than one, since in this case the recovered population is small.

5.2 Analysis of the evolutionary process: global stability, periodicity, and chaos

Thus far, we have seen that a diminished transmission rate of the resident strain leads to the emergence of novel strains characterized by heightened transmissibility rather than increased immune evasion. Conversely, when β is large, the invading strains exhibit an increased capability to evade immunity.

In this section, we direct our attention towards identifying and closely examining the most invasive strain, i.e. the strain with the maximal invasion fitness. Therefore, we focus on answering the question of how this strain can maximize its reproduction number in presence of the resident strain.

To facilitate the mathematical analysis throughout the remainder of this research, we employ a linear trade-off f with transmission advantage parameter a, and cost parameter b representing the expense of immunity evasion: $f(p) = a - bp$, where $0 < a < b$.

In this case, the invasion reproductive number at the endemic steady state of the resident strain can be explicitly expressed as a function of p, and is characterized as a downward parabola of the form $\mathcal{R}(p) = Ap^2 + Bp + C$, where

$$A = -\frac{b\gamma(\beta - (\mu+\gamma))}{\beta(\mu+\gamma)^2}, \qquad B = \frac{\gamma(\beta+a)(\beta-(\mu+\gamma))}{\beta(\mu+\gamma)^2} - \frac{b}{\beta}, \qquad C = \frac{\beta+a}{\beta}.$$

The maximum point of $\mathcal{R}(p)$ is given by

$$p^{\max}(\beta) = \begin{cases} 0, & \beta < \tilde{\beta}_1 \\ \frac{\beta+a}{2b} - \frac{(\mu+\gamma)^2}{2\gamma(\beta-(\mu+\gamma))}, & \tilde{\beta}_1 \leq \beta \leq \tilde{\beta}_2 \\ 1, & \beta > \tilde{\beta}_2, \end{cases} \tag{5.6}$$

where

$$\tilde{\beta}_1 = \frac{\mu+\gamma-a}{2} + \frac{\sqrt{\gamma^2(\mu+\gamma+a)^2 + 4b\gamma(\mu+\gamma)^2}}{2\gamma}$$

and

$$\tilde{\beta}_2 = \frac{\mu+\gamma-a+2b}{2} + \frac{\sqrt{\gamma^2(\mu+\gamma+a-2b)^2 + 4b\gamma(\mu+\gamma)^2}}{2\gamma}.$$

This new fittest strain is characterized by a novel transmission rate denoted as $\beta_v = \beta + a - bp^{\max}$, and from this point on, it takes the place of the resident strain in the system.

Fig. 5.2a presents a graphical representation of the invasion reproduction number $\mathcal{R}(p)$ for three distinct values of the transmission rate β. Each value corresponds to distinct behaviors exhibited by the invasion reproduction function when its maximum value occurs at $p^{\max} = 0$, $p^{\max} = 1$, and $p^{\max} \in (0, 1)$, depicted as filled dots in the figure.

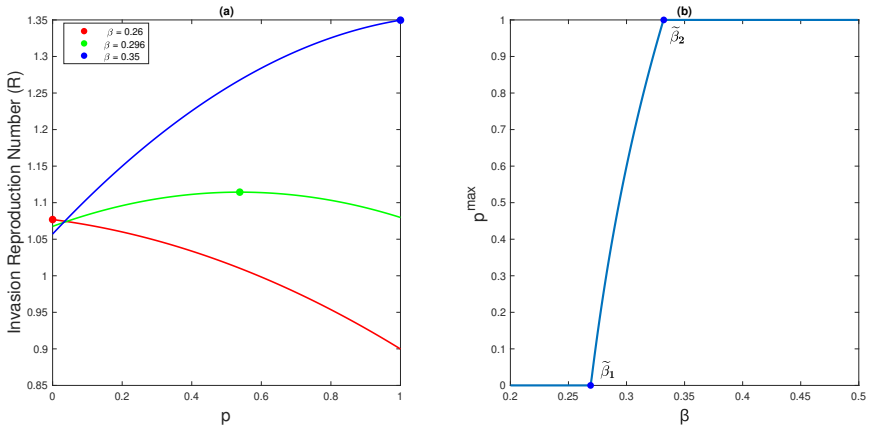

Figure 5.2: *Panel (a) shows the invasion reproduction number with respect to p for three distinct values of the transmission rate parameter β, 0.26, 0.296, and 0.35 (curves red, green, and blue respectively). Each value corresponds to distinct behaviors exhibited by the invasion reproduction function when its maximum value occurs at $p^{\max} = 0$, $p^{\max} = 1$, and $p^{\max} \in (0, 1)$, respectively. Panel (b) shows the function $p^{\max}(\beta)$ with respect to transmission rates of the resident strain. When the transmission rate β surpasses $\tilde{\beta}_2$, the maximum invasion reproduction number exhibits an increasing trend with maximum at $p = 1$ ($p^{\max} = 1$), and for β close enough to $\gamma + \mu$, $p^{\max} = 0$. In both panels, $\mu = 3.5 \cdot 10^{-5}$, $a = 0.02$, $b = 0.1$ and $\gamma = 0.2$.*

By considering $p^{\max}$ as a function of β , the relationship between them is illustrated in Fig. 5.2b. This figure aligns with the implications of Theorem 5.1.1, indicating that as β increases, immune evasion becomes more favorable. Consequently, the invader strain is anticipated to propagate employing a strategy centered around immunity evasion, rather than exhibiting heightened transmissibility.

By iterating this procedure, we obtain a sequence of transmission rates driven by the difference equation

$$\beta_{n+1} = g(\beta_n), \quad \beta_0 > \gamma + \mu, \tag{5.7}$$

where $g : (\gamma + \mu, \infty) \to (\gamma + \mu, \infty)$,

$$g(\beta) = \begin{cases} \beta + a, & \text{if } \beta < \tilde{\beta}_1; \\ \frac{\beta+a}{2} + \frac{b(\mu+\gamma)^2}{2\gamma(\beta-(\mu+\gamma))}, & \text{if } \tilde{\beta}_1 \leq \beta \leq \tilde{\beta}_2; \\ \beta + a - b, & \text{if } \beta > \tilde{\beta}_2. \end{cases} \tag{5.8}$$

The following proposition contains some basic properties of the map g, which can be verified by straightforward calculation.

Proposition 5.2.1. *For any $b > a > 0$, function g defined in* (5.8)*,*

(i) possesses a unique fixed point $\beta^* \in (\tilde{\beta}_1, \tilde{\beta}_2)$ *defined as*

$$\beta^* = \frac{a+\mu+\gamma}{2} + \frac{\sqrt{\gamma^2 a(a-2(\mu+\gamma)) + \gamma(4b+\gamma)(\mu+\gamma)^2}}{2\gamma}, \tag{5.9}$$

(ii) is linear and strictly increasing with constant slope 1 *within the intervals* $(\gamma+\mu, \tilde{\beta}_1]$ *and* $[\tilde{\beta}_2, \infty)$*,*

(iii) is convex on $[\tilde{\beta}_1, \tilde{\beta}_2]$*, moreover, it is strictly decreasing on* $(\tilde{\beta}_1, \beta_{\min})$ *and strictly increasing on* $(\beta_{\min}, \tilde{\beta}_2)$*, where* $\beta_{\min} \in [\tilde{\beta}_1, \tilde{\beta}_2]$ *is defined by*

$$\beta_{\min} = \begin{cases} \gamma+\mu+\sqrt{\frac{b(\gamma+\mu)^2}{\gamma}}, & \text{if } b > \frac{a+\gamma+\mu}{2} \\ \tilde{\beta}_2, & \text{if } a < b \leq \frac{a+\gamma+\mu}{2}. \end{cases} \tag{5.10}$$

In the following subsections, we demonstrate a variety of behaviors, from stability, through periodicity, to chaos.

5.2.1 Global Convergence

Through the mathematical framework presented below, Theorem 5.2.2, we investigate the conditions under which transmissibility is stabilized, implying that over the long term, emerging variants will have approximately the same transmission rate. We illustrate this by providing explicit conditions under which the emergence of forthcoming strains, characterized by the sequence of transmission rates $\{\beta_n\}$, converges to the fixed point.

Theorem 5.2.2. *The unique fixed point* β^* *of the difference equation* (5.7) *is*

(i) locally asymptotically stable (LAS) if

$$b > a > \gamma+\mu \quad \text{or} \quad b > \max\left\{a, \frac{3\gamma(\gamma+\mu-a)^2}{4(\gamma+\mu)^2}\right\};$$

(ii) locally unstable if $a < b < \frac{3\gamma(\gamma+\mu-a)^2}{4(\gamma+\mu)^2}$ *and* $a \leq \gamma+\mu$*;*

(iii) globally asymptotically stable (GAS) (i.e. LAS and globally attractive) if

$$b > a > \gamma+\mu \ \text{ or } \ b > \max\left\{a, \frac{3\gamma(\gamma+\mu-a)^2}{4(\gamma+\mu)^2}, \frac{3\gamma(-a^2+4(\gamma+\mu)^2)}{16(\gamma+\mu)^2}\right\}.$$

Before we prove Theorem 5.2.2, let us recall some results and tools related to local and global stability.

Theorem 5.2.3 ([6, Theorem 2.1]). *If x^* is a fixed point of $f : (c, d) \to (c, d)$, then the fixed point is locally asymptotically stable if $|f'(x^*)| < 1$, and locally unstable if $|f'(x^*)| > 1$.*

Definition 5.2.4 ([27]). *A function $\phi(x)$ envelops a function $f(x)$ on the interval (c, d) if and only if for the unique fixed point x^**

$$(1)\ \phi(x) > f(x) \quad \textit{for } x \in (c, x^*), \quad \textit{and} \quad (2)\ \phi(x) < f(x) \quad \textit{for } x \in (x^*, d).$$

Theorem 5.2.5 ([28, Theorem 3]). *Assume that f maps the open interval (c, d) into itself. (The map $f(x)$ may be discontinuous and/or multi-valued). Furthermore, assume that $f(x^*) = x^*$ is the unique fixed point of f, and that there is a continuous self-inverse function $\phi(x)$ which envelops $f(x)$ on (c, d). Then if x_0 is any initial point and $\{x_n\}$ is any sequence consistent with $x_{t+1} = f(x_t)$, then $\{x_n\}$ converges to x^*.*

Proof of Theorem 5.2.2. (i) From Theorem 5.2.3, the local asymptotic stability of the function $g(\beta)$ is established when the condition $|g'(\beta^*)| < 1$ is satisfied. An elementary calculation shows that if $a > \gamma + \mu$, then $g'(\beta^*) \in (0, 1)$. Moreover, if $b > \frac{3\gamma(\gamma+\mu-a)^2}{4(\gamma+\mu)^2}$ and $a \leq \gamma + \mu$, then $g'(\beta^*) \in (-1, 0)$, concluding the proof of statement (i).

(ii) Similarly, when $a < b < \frac{3\gamma(\gamma+\mu-a)^2}{4(\gamma+\mu)^2}$ and $a \leq \gamma + \mu$, then $g'(\beta^*) < -1$. Thus, according to Theorem 5.2.3, the fixed point is locally unstable.

(iii) Assume that the condition of statement (iii) holds. To establish global stability, in view of Theorem 5.2.5 and statement (i), it suffices to construct a suitable function which envelopes the function g. To accomplish this, we introduce the self-inverse function $\phi(\beta) = 2\beta^* - \beta$. We claim that ϕ is an enveloping function for g on $(\gamma + \mu, \infty)$. Without loss of generality, we show that ϕ envelopes function g over the interval $(\tilde{\beta}_1, \tilde{\beta}_2)$ (since ϕ is strictly decreasing and $g(\tilde{\beta}_1) > g(\beta)$ for $\beta < \tilde{\beta}_1$, and $g(\tilde{\beta}_2) < g(\beta)$, when $\tilde{\beta}_2 < \beta$). Given that the function g is convex on $[\tilde{\beta}_1, \tilde{\beta}_2]$, $\phi' \equiv -1$, and $g'(\beta^*) > -1$, hence, to fulfill the first condition of Definition 5.2.4, it suffices to show that $g(\tilde{\beta}_1) < \phi(\tilde{\beta}_1)$. This inequality holds exactly when $b > \frac{3\gamma(-a^2+4(\gamma+\mu)^2)}{16(\gamma+\mu)^2}$.

Finally, this condition always holds when $b > a > \gamma + \mu$, because $\gamma + \mu > \frac{3\gamma(-a^2+4(\gamma+\mu)^2)}{16(\gamma+\mu)^2}$. This completes the proof of statement (iii). □

Fig. 5.3 shows that $g(\beta)$ is enveloped by the linear function $\phi(\beta) = 2\beta^* - \beta$. In this example, we have $a > \mu + \gamma$, thus global asymptotic stability follows from Theorem 5.2.2.

Fig. 5.4a illustrates the bifurcation diagram of the function $g(\beta)$ with b serving as the bifurcation parameter. This diagram reveals how varying the parameter b leads to changes in solutions of the difference equation (5.7), representing the sequence of transmission rates of emerging fittest strains. The pink and orange lines mark the critical points of b for local and global stability, respectively (under the condition $a < \gamma+\mu$). Surpassing the threshold of local stability given by Theorem 5.2.2(i), solutions demonstrate convergence towards the fixed point. This means, over a sufficiently long period, all prevailing strains will practically have the same transmission rate.

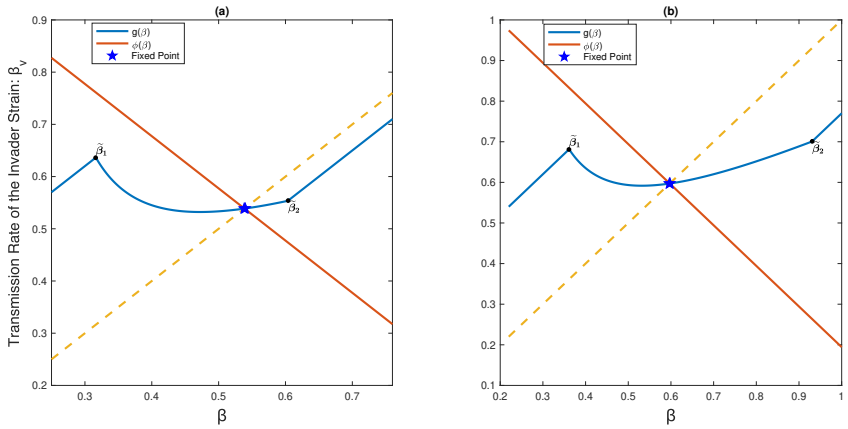

Figure 5.3: *Graph of* $g(\beta) = \beta + a - bp^{\max}$ *plotted with the enveloping function* $\phi(\beta) = 2\beta^* - \beta$ *(red line) and identity line* $\beta_v = \beta$ *(dashed line). In panel (a), the parameter* $b = a + 0.05$ *is chosen such that* $g(\tilde{\beta}_1) > g(\tilde{\beta}_2)$*, and in panel (b),* $g(\tilde{\beta}_1) < g(\tilde{\beta}_2)$ *for* $b = 0.55$*. In this example,* $a = 1.6(\gamma + \mu) > \mu + \gamma$*, thus global asymptotic stability follows from Theorem 5.2.2. Other parameters are* $\gamma = 0.2$*,* $\mu = 3.5 \cdot 10^{-5}$*.*

This is also illustrated in Fig. 5.5a, where any chosen initial point leads to a solution converging to this fixed point. These numerical evidences indicate that the notable gap between the mentioned thresholds (cf. statements (i) and (ii) of Theorem 5.2.2) could be filled. In other words, we conjecture that local asymptotic stability of the fixed point in fact implies its global stability. In the bifurcation diagram, a lower punishment (cost) parameter b is associated with increased complexity in behavior, as detailed in Section 5.2.3.

Fig. 5.4b also illustrates the bifurcation diagram for the immune evasion parameter p via equation (5.6), with b serving as the bifurcation parameter. When b reaches a value where the system exhibits a two-periodic transmission rate, $p^{\max}$ also alternates between two values: $p^{\max} = 0$ and some $p^{\max} \in (0, 1)$. This means that strains with a higher transmission rate will be followed by a strain having smaller transmission rate but with the ability to potentially reinfect a significant proportion of the recovered population (30–50% in this parameter region). Conversely, strains with lower β will be followed by $p^{\max} = 0$, where the next strain will have the advantage of having a higher transmission rate, but in return, it will not be able to reinfect individuals recovered from the previous strain at all.

5.2.2 Attracting Interval

In the upcoming theorem, we identify an interval into which all solutions of the difference equation (5.7) enter and do not leave thereafter. This implies that, over an extended period, the transmission rates of the new strains remain within this specified interval.

Theorem 5.2.6. *Let* $\beta_+ > \sup g\big((\gamma + \mu, \beta^*]\big)$ *and* $\gamma + \mu < \beta_- < \inf g\big([\beta^*, \beta_+]\big)$*. Then*

$g\big([\beta_-, \beta_+]\big) \subseteq [\beta_-, \beta_+]$*, and every solution of* (5.7) *enters* $[\beta_-, \beta_+]$ *without leaving it again.*

Proof. This theorem is a direct application of Proposition 9.5 of [77]. □

Remark 5.2.7. *The supremum of the function* g *on* $(\gamma + \mu, \beta^*]$ *is easily observed to be* $g(\tilde{\beta}_1) = \tilde{\beta}_1 + a$*. The determination of the infimum depends on the parameters and may manifest as* $g(\tilde{\beta}_1 + a)$*, or* $g(\beta_{\min})$*, where* $\beta_{\min}$ *was defined in* (5.10)*.*

When $\tilde{\beta}_1 + a < \beta_{\min}$*,* β_- *can be chosen arbitrarily from* $(\gamma + \mu, g(\tilde{\beta}_1 + a))$*. Conversely, for instances where* $\tilde{\beta}_1 + a \geq \beta_{\min}$*,* β_- *can be selected arbitrarily within the interval* $(\gamma + \mu, g(\beta_{\min}))$*.*

We depict the bounded interval, denoted as $[\beta_-, \beta_+]$, within the bifurcation diagram showcased in Fig. 5.4a. This illustration offers a visual confirmation that the transmission rates associated with the newly emerging strain will persist within this designated interval over an extended period.

5.2.3 Periodic Solutions and Complex Dynamics

In this section, we demonstrate that, in cases where the fixed point is locally unstable, there is at least one two-periodic solution. This is observed in the depicted solutions presented in Fig. 5.4a and 5.5b for specific values of the parameter b. These findings indicate that, despite multiple iterations and the emergence of numerous subsequent strains, only two transmission rates are repeated alternately in the system over the long term. In addition, within Theorem 5.2.13, we demonstrate that the difference equation (5.7), under specific conditions, exhibits chaotic behavior. This implies that the system's dynamics is unpredictable, making it challenging to forecast whether the emergence of the next strain will be attributed to a heightened transmission rate or its capability to evade the immune system.

Theorem 5.2.8. *If* $a < b < \frac{3\gamma(\gamma+\mu-a)^2}{4(\gamma+\mu)^2}$ *and* $a \leq \gamma + \mu$*, then, there exists at least one two-periodic solution of the difference equation* (5.7) *different from* β^**.*

To prove this theorem, we use the following concepts and results of [77].

Assumption 1. *The function* $f : (c, \infty) \to (c, \infty)$ *is continuous, with a unique fixed point* $x^* > c$*, and is bounded on* (c, ∞)*. Moreover, there exist* x_1 *and* x_2*,* $c < x_1 < x^* < x_2 < \infty$*, such that* $f(x_1) > x_1$ *and* $f(x_2) < x_2$*.*

Theorem 5.2.9 ([77, Theorem 9.6])**.** *Assume that Assumption 1 holds and there is no fixed point of* f^2 *different from the unique fixed point* x^**. Then all solutions of the difference equation* $x_{n+1} = f(x_n)$*, i.e.* $\{x_n\}$ *with* $n \in \mathbb{N}$ *with* $x_0 > c$*, converge to* x^**, as* $n \to \infty$*.*

Definition 5.2.10. *For any* $y \in (c, \infty)$*, let* $M_-(y)$ *represent the set of initial conditions* x *that are mapped onto* y *by the iterative application of the function* f*, i.e.*

$$M_-(y) = \bigcup_{n=1}^{\infty} \{x \in (c, \infty) : f^n(x) = y\}.$$

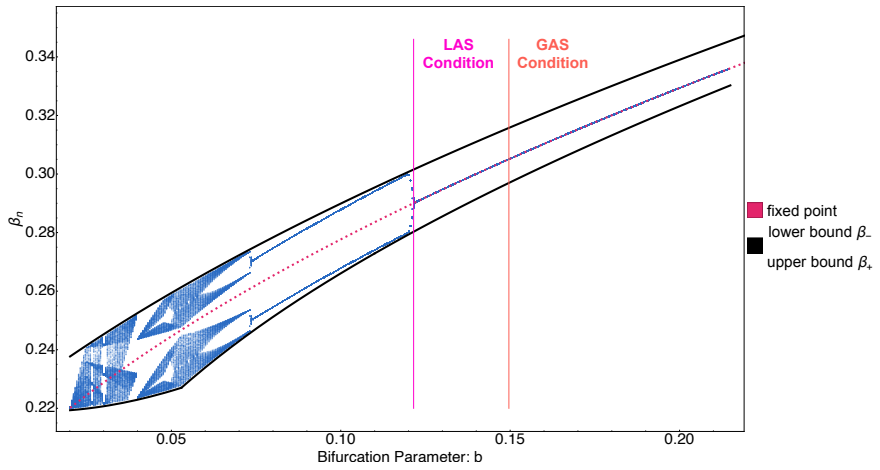

(a) *Bifurcation diagram for the difference equation* (5.7). *The diagram captures the diverse behaviors—chaotic, periodic, and convergent—across a range of values for* b. *On the left side of the "LAS Condition"-line, the fixed point is unstable and on the right side of the "GAS Condition"-line, the fixed point is globally asymptotically stable (Theorem 5.2.2(iii)). All trajectories are confined within the interval* $[\beta_-, \beta_+]$ *(Theorem 5.2.6 and Remark 5.2.7).*

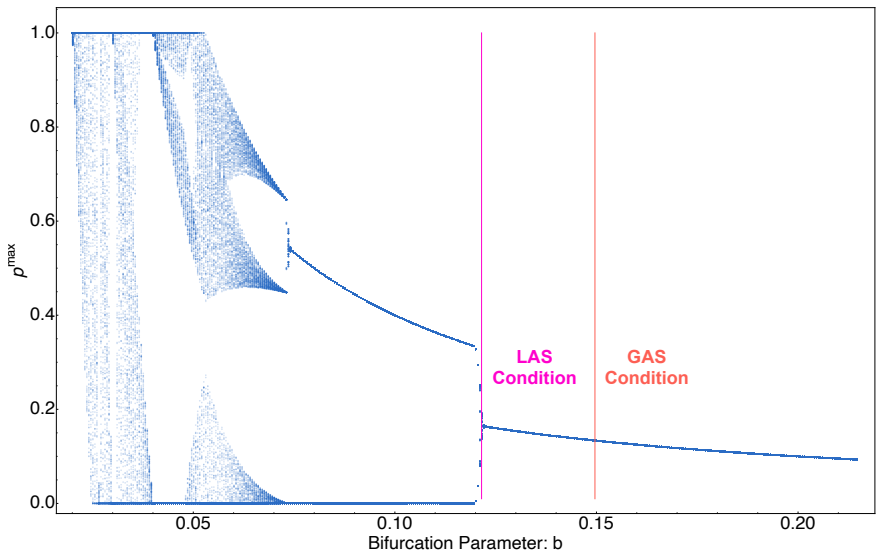

(b) *Bifurcation diagram for immune evasion* p *via the equation* (5.6).

Figure 5.4: *Bifurcation diagram for the equations* (5.7) *and* (5.6). *The system was iterated for* $n = 1000$ *steps from ten initial values for each* b *in between* 0.02 *and* 0.21 *with step-size* 0.0005, *and the last* 50 *iterations are displayed in the plot. Here,* $\mu = 3.5 \cdot 10^{-5}$, $\gamma = 0.2$, *and* $a = 0.02$.

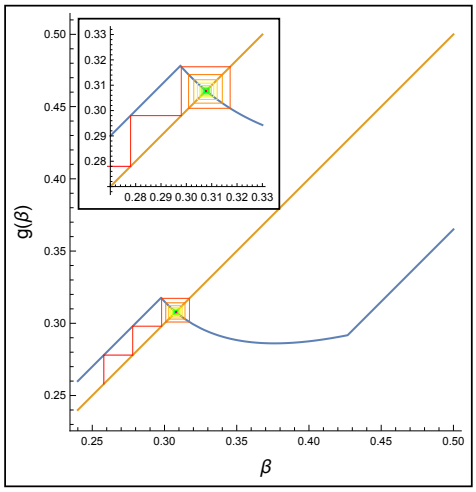

(a) *Cobweb plot for* (5.7) *with initial value* $\beta = 0.258$ *and parameter* $b = 0.155$ *tends to the unique fixed point. This diagram illustrates the case when the fixed point* β^* *is globally asymptotically stable.*

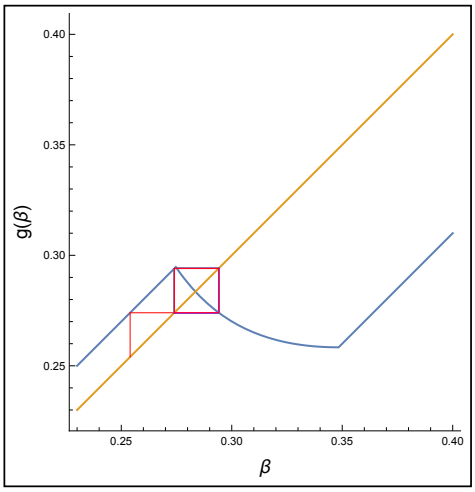

(b) *The cobweb plot with initial value* $\beta = 0.254$ *and* $b = 0.11$ *illustrates the manifestation of a two-cycle within the system. With multiple iterations, only two transmission rates are repeated alternately.*

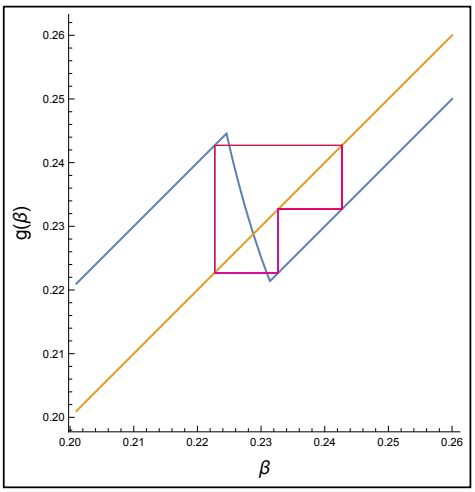

(c) *The cobweb plot, initialized with* $\beta = 0.2227$ *and parameter* $b = 0.03$*, reveals a 3-periodic solution, as also proved in Theorem 5.2.13.*

Figure 5.5: *The cobweb plots correspond to three distinct behaviors of* (5.7)*.* $\mu = 3.5 \cdot 10^{-5}$*,* $\gamma = 0.2$*, and* $a = 0.02$

Proposition 5.2.11 ([77, Proposition 9.11])**.** *Assume that $f^{-1}(\{x\})$ is countable for every $x \in (c, \infty)$. Then $M_-(y)$ is countable for every point $y \in (c, \infty)$.*

Remark 5.2.12. *Assumption 1, Theorem 5.2.9 and Definition 5.2.10 provided above, are found in [77] with $c = 0$. However, this can be easily addressed through a trivial change of variables.*

Now, we are in position to prove Theorem 5.2.8.

Proof of Theorem 5.2.8. Considering Theorem 5.2.9 and the fulfillment of Assumption 1, it is adequate to demonstrate the existence of a solution that does not converge to β^*. According to Theorem 5.2.2, when $a < b < \frac{3\gamma(\gamma+\mu-a)^2}{4(\gamma+\mu)^2}$ and $a \leq \gamma + \mu$, β^* is locally unstable and $g'(\beta^*) < -1$. Since $\beta^* \in (\tilde{\beta}_1, \tilde{\beta}_2)$, so g' is continuous in a small neighborhood of the fixed point, therefore, there exists some $\epsilon \in (0, \beta^* - (\gamma+\mu)]$ such that $g'(\beta) < -1$ for all $\beta \in (\beta^* - \epsilon, \beta^* + \epsilon)$. Furthermore, since any point $\beta \in (\gamma+\mu, \infty)$ has a countable inverse set, more precisely, the cardinality of the set $g^{-1}(\{\beta\})$ is at most three (see Proposition 5.2.1 (ii)–(iii)), it follows that the set $M_-(\beta)$ is also countable as per Proposition 5.2.11. Consequently, there exists $\beta_0 \in (\gamma + \mu, \infty)$, such that $\beta_0 \notin M_-(\beta^*)$. Assuming to the contrary that $\lim_{n\to\infty} \beta_n = \beta^*$, there exists some $m \in \mathbb{N}$ such that $|\beta_n - \beta^*| < \epsilon$ for all $n \geq m$ and $\beta_n \neq \beta^*$, since $\beta_0 \notin M_-(\beta^*)$. However, by the mean value theorem, for all $n \geq m$, $|\beta_{n+1} - \beta^*| = |g(\beta_n) - g(\beta^*)| = |g(\xi_n)||\beta_n - \beta^*| > |\beta_n - \beta^*| > 0$ holds for some ξ_n between β^* and β_n. This contradicts the convergence of β_n towards β^*, proving our statements. □

Theorem 5.2.13. *Let $0 < a < b$. If $g(\tilde{\beta}_1 + a) \leq \tilde{\beta}_1 - a$ or $\tilde{\beta}_2 + b - a \leq g(\tilde{\beta}_2 + a - b)$ holds, then the difference equation* (5.7) *is chaotic in the sense of Li and Yorke [46], i.e.*

1. *for every positive integer k there is a periodic point in $(\gamma + \mu, \infty)$ having period k;*
2. *there is an uncountable set $S \subseteq (\gamma + \mu, \infty)$ with no periodic points which satisfies the following conditions:*

   (i) for every $p, q \in S$ with $p \neq q$,

   $$\limsup_{n\to\infty} |g^n(p) - g^n(q)| > 0 \quad \textit{and} \quad \liminf_{n\to\infty} |g^n(p) - g^n(q)| = 0;$$

   (ii) for every $p \in S$ and periodic point $q \in (\gamma + \mu, \infty)$,

   $$\limsup_{n\to\infty} |g^n(p) - g^n(q)| > 0.$$

Proof. By virtue of [46, Theorem 1] it suffices to identify a β_0 that fulfills condition $g^3(\beta_0) \leq \beta_0 < g(\beta_0) < g^2(\beta_0)$ or $g^3(\beta_0) \geq \beta_0 > g(\beta_0) > g^2(\beta_0)$.

When $g(\tilde{\beta}_1 + a) \leq \tilde{\beta}_1 - a$, then let $\beta_0 = \tilde{\beta}_1 - a$. Note that, since g maps the interval $(\gamma + \mu, \infty)$ into itself, $\gamma + \mu < \beta_0$ must hold. Then the inequalities

$$\beta_0 < g(\beta_0) = \tilde{\beta}_1 < \tilde{\beta}_1 + a = g^2(\beta_0) \quad \text{and} \quad g^3(\beta_0) = g(\tilde{\beta}_1 + a) \leq \tilde{\beta}_1 - a = \beta_0$$

clearly hold, so $g^3(\beta_0) \leq \beta_0 < g(\beta_0) < g^2(\beta_0)$ is satisfied.

Similarly, if $\tilde{\beta}_2 + b - a \leq g(\tilde{\beta}_2 + a - b)$ is fulfilled, then setting $\beta_0 = \tilde{\beta}_2 + b - a$ leads to

$$\beta_0 > g(\beta_0) = \tilde{\beta}_2 > \tilde{\beta}_2 + a - b = g^2(\beta_0)$$

and

$$g^3(\beta_0) = g(\tilde{\beta}_2 + a - b) \geq \tilde{\beta}_2 + b - a = \beta_0,$$

that is, $g^3(\beta_0) \geq \beta_0 > g(\beta_0) > g^2(\beta_0)$ holds, just as required. □

Corollary 5.2.14. *If either* $\tilde{\beta}_2 - \tilde{\beta}_1 \leq a \leq \frac{b}{3}$ *or* $a + \tilde{\beta}_2 - \tilde{\beta}_1 \leq b \leq \frac{3a}{2}$ *is satisfied, then the difference equation* (5.7) *is chaotic in the sense of Li and Yorke.*

Proof. Assuming $\tilde{\beta}_2 - \tilde{\beta}_1 \leq a \leq \frac{b}{3}$ yields $g(\tilde{\beta}_1 + a) = \tilde{\beta}_1 + 2a - b \leq \tilde{\beta}_1 - a$, while condition $a + \tilde{\beta}_2 - \tilde{\beta}_1 \leq b \leq \frac{3a}{2}$ immediately implies $g(\tilde{\beta}_2 + a - b) = \tilde{\beta}_2 + 2a - b \geq \tilde{\beta}_2 + b - a$. Hence, conditions of Theorem 5.2.13 are satisfied in both cases. □

A straightforward implication of Theorem 5.2.13 is the existence of a three-periodic solution. Fig. 5.5c offers numerical validation of this phenomenon, presenting evidence that corroborates the theoretical predictions made by the theorem.

Fig. 5.6 illustrates four distinct regions, each representing a different dynamical behavior of the equation (5.7). The blue and yellow regions denote the domains where the fixed point is globally and locally asymptotically stable, respectively, whereas the green region highlights areas of instability where 2-periodic orbits emerge, as delineated in Theorems 5.2.2 and 5.2.8. The gray region (obtained in Theorem 5.2.13 (gray) and Corollary 5.2.14 (light gray region)) reflects the chaotic aspects of the difference equation (5.7), within which predicting the behavior of subsequent strains becomes challenging.

Fig. 5.7 illustrates the prevalence of infection for each strain within the context of the presented Model (2.1), following the scheme presented in Fig. 5.1 This illustrative figure was constructed by integrating the SIR model, and when the solution approached the endemic steady state, we switched to a new strain (i.e., new β) selected by maximizing invasion fitness via the trade-off. Depending on the immune evasion parameter p of the new strain, we reallocated recovered and susceptible individuals to create the initial state for the next period. Then we repeated the procedure by newer and newer strains.

Panel (a) corresponds to the conditions outlined in Theorem 5.2.2, where the transmission rates of strains converge to an equilibrium. Under these conditions, a stable transmission rate ensures a uniform steady-state prevalence across all strains. As observed, the infection levels for all strains remain consistent over time, showing a stable and predictable pattern of infection dynamics.

Panel (b) corresponds to a stable 2-periodic scenario. After the first wave, we experience a fast convergence in the trajectory of the dynamics of transmission rates to a 2-periodic pattern. This periodicity in transmissibility leads to alternating prevalence levels. Higher prevalence corresponds to a greater proportion of the infected population, indicating a more harmful evolutionary outcome.

In panel (c) each strain possesses a different transmission rate, resulting in a highly irregular and unpredictable pattern of infection prevalence. This behavior corresponds to the chaotic regime of the difference equation (5.7). The figure highlights how variations in transmissibility across strains can drive complex outcomes in infection prevalence, making it challenging to predict long-term dynamics.

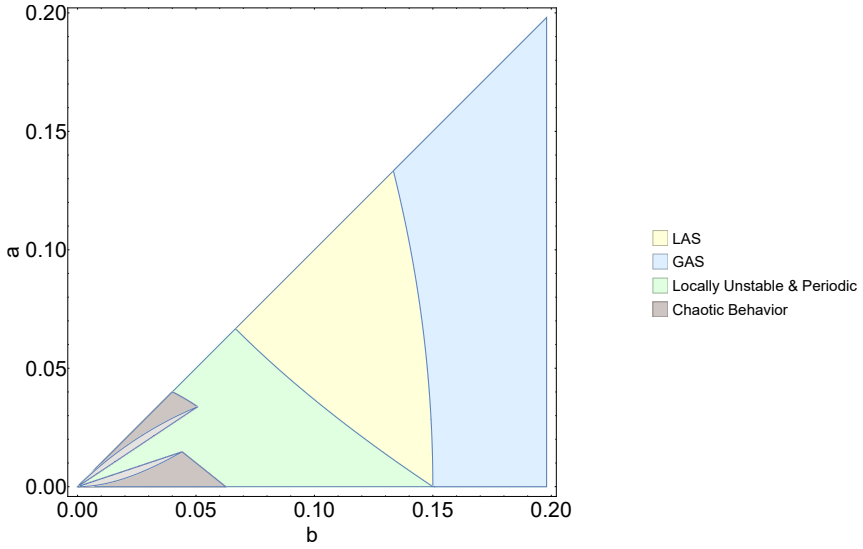

Figure 5.6: *The figure delineates four distinct regions, each corresponding to a unique dynamical behavior of the system as defined by the difference equation* (5.7). *The regions colored in blue and yellow represent domains where the fixed point exhibits global and local asymptotic stability, respectively. The green regions are zones of instability, as given in Theorem 5.2.2. The area depicted in gray encapsulates chaotic dynamics of* (5.7). *Here* $\gamma = 0.2$ *and* $\mu = 3.5 \cdot 10^{-5}$.

5.3 Discussion

Gaining insights into the evolution of pathogens' traits is significant not only in the context of evolutionary dynamics but also holds crucial implications for epidemiology and public health. These evolutionary traits include virulence, transmission efficiency, replication rate, resistance to stress and antimicrobials, etc. Mechanisms that allow pathogens to avoid, suppress, or manipulate the host's immune system are also vital for their long term survival. Understanding the evolution of host immune evasion is central to designing influenza vaccines, since influenza strains in subsequent years may evade prior immunity [19, 33], and this issue gained attention during the COVID-19 pandemic as well [73].

The evolution of these traits is often intertwined via various trade-offs. Most notably, the trade-off between virulence and transmissibility has been investigated in numerous research papers. In comparison, the immune evasion–transmissibility

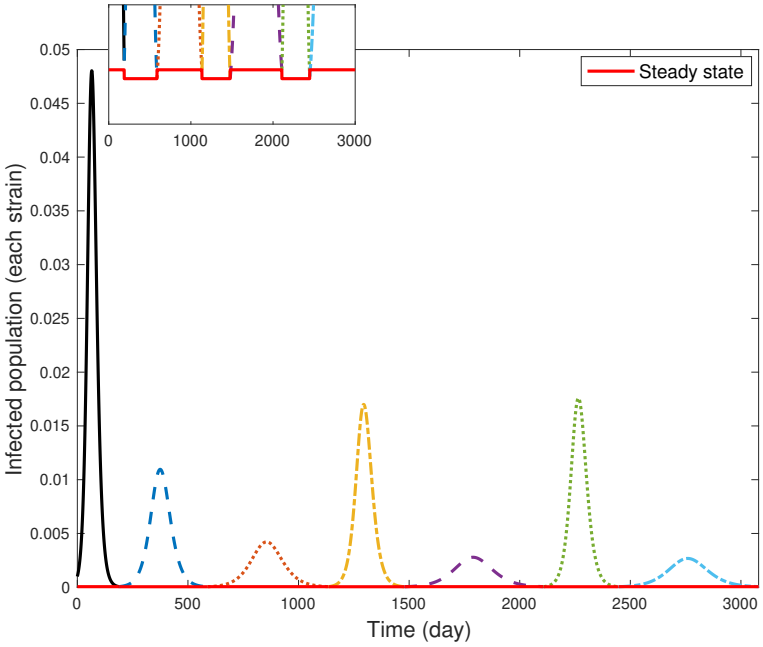

(a) *Stable transmission rates yield similar waves and the same prevalence at steady state (shown in the inset) across subsequent strains. Here* $b = 0.208$*,* $\beta = 0.404$*, and* $a = 0.2$*.*

Figure 5.7: *Prevalence dynamics of infection under varying transmission rate scenarios. The initial value of* S*,* I*, and* R *are* 0.999*,* 0.001*, and* 0 *respectively;* $\mu = 3.5 \cdot 10^{-5}$*,* $\gamma = 0.2$*.*

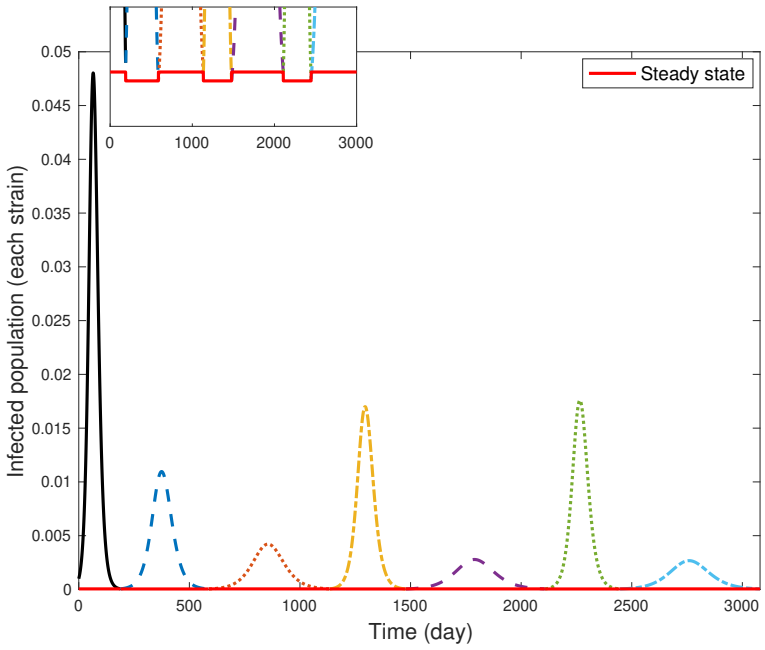

(b) *Two periodic trajectory of transmission rates result in alternating smaller and larger outbreak. Periodicity of prevalence at steady state shown in the inset. Here* $b = 0.083$*,* $\beta = 0.282$*, and* $a = 0.05$*.*

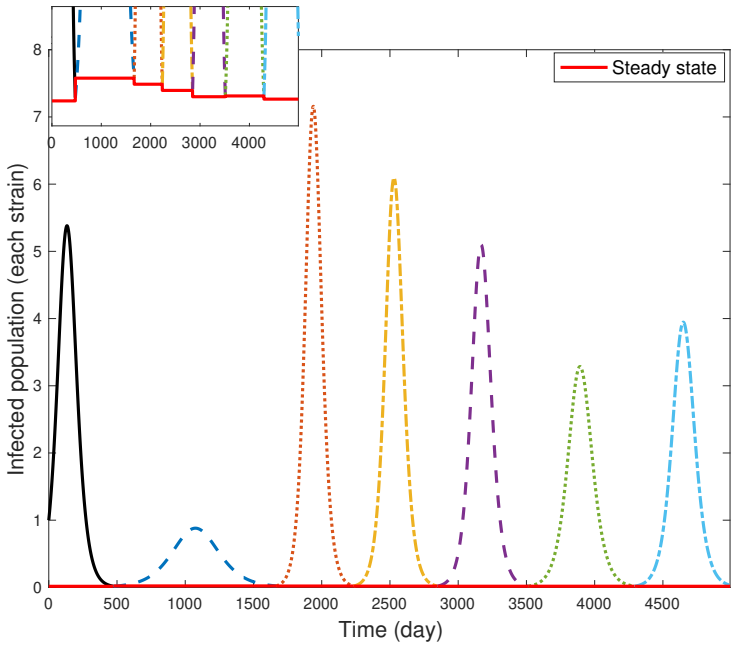

(c) *Variable transmission rates produce chaotic infection dynamics. Here* $b = 0.0223$*,* $\beta = 0.220$*, and* $a = 0.02$*.*

Figure 5.7: *Prevalence dynamics of infection under varying transmission rate scenarios. The initial value of* S*,* I*, and* R *are* 0.999*,* 0.001*, and* 0 *respectively;* $\mu = 3.5 \cdot 10^{-5}$*,* $\gamma = 0.2$*.*

trade-off received less attention, and has not been explicitly considered in mathematical models of viral evolution. By incorporating this trade-off into a novel evolutionary model, we explored the emergence of new variants and their long term evolutionary patterns.

Our starting point was an epidemiological Model (2.1) considering a single resident strain. Novel strains emerge with a transmission rate denoted by $\beta_v = \beta + f(p)$, where $p \in [0, 1]$ is the immune-evasion, and $f(\cdot)$ is a decreasing function expressing the trade-off. Strains with $p = 0$ lack the ability to evade the immune response in individuals who have acquired immunity and currently belong to the recovered (R) compartment. Conversely, strains with $p = 1$ are capable of infecting all individuals who have recovered from the previous strain. As demonstrated in Theorem 5.1.1, when the transmission rate of the resident strain, β, is sufficiently close to $\gamma + \mu$, the invasion reproduction number $\mathcal{R}(p)$ decreases across the range of p. Consequently, the new strain exhibits a higher transmission rate, and invasion fitness is maximized at $p = 0$. Conversely, for cases where $\beta \gg (\gamma + \mu)$, immune evasion becomes advantageous and invasion fitness is maximized at $p = 1$. For intermediate values of β, invasion fitness is maximized at some $0 < p < 1$.

We assume that evolution selects the most invasive strain (with maximal invasion reproduction number), characterized by a transmission rate $\beta_v = \beta + f(p^{\max})$. This new variant replaces the resident strain, and we let the system into the new endemic steady state, initiating a cycle of strain replacements. This process can be reduced mathematically to a difference equation (see (5.7)). For the sake of analytic results, we focused on a linear trade-off function $f(p) = a - bp$. Our findings reveal that this methodological simplification does not compromise the complexity of the observed dynamics, which range from the global stability of the fixed point to the emergence of periodic and even chaotic behavior.

To find conditions for the global stability of the unique fixed point of (5.7), we applied the enveloping technique of [27]. Our investigation uncovered that, within a specific parameter range for b, the fixed point is globally asymptotic stable. This suggests that over time, new variants consistently exhibit similar intrinsic transmission rates of infection. Additionally, our analysis has demonstrated that the emergence of instability is accompanied by both periodic and chaotic behaviors. Specifically, Theorem 5.2.6 establishes the existence of at least one two-periodic solution, suggesting that the system can alternate between only two transmission rates over extended periods. Theorem 5.2.13 delineates the conditions under which the solutions of the difference equation (5.7) exhibit chaotic behavior. This chaotic nature renders the system's dynamics inherently unpredictable in the long run. These diverse behaviors are visually represented in Fig. 5.6, where each colored region corresponds to one of the following dynamics of the equation (5.7): GAS, LAS, locally unstable, and chaotic/periodic. Bifurcation diagram 5.4a and cobweb plot 5.5 offer a visualization of the evolution of the given model across successive iterations, depicting its dynamics from an initial value. In Fig. 5.5a (and a segment of Fig. 5.4a), the convergence to the fixed point is evident, however, it is not universal. When the conditions outlined in Theorem 5.2.2 are not met, the system may exhibit periodic and

even chaotic behaviors, as depicted in Figs. 5.5b, 5.5c, and the left side of Fig. 5.4a, for $b < \frac{3\gamma(\gamma+\mu-a)^2}{4(\gamma+\mu)^2}$. In the bifurcation diagram, one can see that reducing the cost parameter b is directly correlated with an escalation in behavioral complexity. This dynamics fosters a more unpredictable and complex pattern of viral evolution. As it was observed during the pandemic, SARS-CoV-2 viral evolution is inherently unpredictable [22]. Our results offer a mechanism via a simple trade-off that naturally leads to such unpredictability.

Naturally, there are several limitations to this approach. To focus on the impact of the transmissibility/immune evasion trade-off, we ignored other complex phenomena that influence the disease transmission dynamics, and restricted ourselves to a simple SIR model. We assumed that the most invasive strain replaces the resident strain. This is a strong assumption which simplifies our framework, but it might not capture the full range of potential evolutionary behaviors. For instance, relaxing this assumption could lead to scenarios where multiple strains co-circulate with significant prevalences, or where the success of invasion is influenced by factors such as host immune landscapes, heterogeneity in immunity in the population, or other selection pressures. Additionally, we ignored superinfection, competition between multiple strains, or immune memory from previous infections, which could alter the observed dynamics. However, in the context of SARS-CoV-2 evolution during the COVID-19 pandemic, in the first few waves we have not observed significant coexistence of strains (see Fig 3.7, for example). Instead, new variants have quickly and consistently outcompeted the previous strains and established dominance, as seen with the successive emergence of variants like Alpha and Delta. This offers that, at least for this particular scenario, the evolutionary trajectory aligns with the dominance of the fittest strain, possibly driven by its higher transmissibility or immune evasion capabilities. Nevertheless, our results point out that assuming such simple mechanisms and even a linear trade-off can lead to complicated dynamics.

Predicting the emergence of new viral strains is a major challenge. Our results indicate that even under a simplified model, where we assume a linear trade-off between transmissibility and immune evasion, the dynamics of strain emergence can be highly unpredictable and even chaotic in certain conditions. This suggests that, despite the simplicity of our model, the emergence of new strains can exhibit complex and erratic behaviors for a range of pathogens as well. Such findings highlight the inherent unpredictability in viral evolution, which is especially relevant when considering real-world scenarios, such as the evolution of SARS-CoV-2 during the pandemic.

Future research may consider more complicated disease dynamics models, in particular, our method is applicable to any compartmental model (which may include even differential delay equations) that has a unique, globally asymptotically stable endemic equilibrium. It would also be interesting to study other functional forms of trade-off, or multiple trade-offs between various traits. This way one can potentially assess the robustness of these results as well as gain further insight into viral evolution. Furthermore, the bifurcation diagram in Fig. 3.2 suggests that our result on global stability in Theorem 5.2.2 is not sharp. A potential avenue for future research

is the application of different enveloping functions, which may result in sharper conditions for global stability. We conjecture that local stability of the equilibrium of the difference equation (5.7) always implies its global stability as well.

Summary

This thesis addresses two pivotal aspects of infectious disease dynamics: the development of mathematical models for disease spread and the exploration of immunity's role in viral evolution.

We investigate epidemic patterns of emerging variants under dynamic social distancing measures. We study the various patterns that are generated under different assumptions of cross-immunity. If recovery from a given strain provides immunity against all previous strains, but not against more novel strains, then we observe a very regular sequential pattern of strain replacement where newer strains predominate over older strains. However, if protection upon recovery holds only against that particular strain and none of the others, we find much more complicated dynamics with potential recurrence of earlier strains, and co-circulation of various strains. We also compare the observed patterns with genomic analysis we have seen during the COVID-19 pandemic in the Netherlands.

Network-based approaches to disease transmission are then explored using stochastic models within network structures, with a focus on the SIR model. This includes analyzing the dynamics of virus spread across various networks to investigate the impact of network structure on disease propagation. We also examine the effect of viral mutations and immunity on transmission patterns and evaluate the efficacy of global social distancing strategies in controlling outbreaks. We show how the strategic timing of implementing global social distancing measures is pivotal in the effective management of infectious disease outbreaks.

Further, gaining insights into the trade-off between pathogens' traits is significant not only in the context of evolutionary dynamics but also holds crucial implications for epidemiology and public health. In Chapter 5 we aim to investigate the implications of a trade-off between immune evasion and transmissibility, motivated by COVID-19, but potentially applicable to other infectious diseases as well. While other trade-offs (most commonly between transmissibility and virulence) have been widely studied and discussed in the literature, immune evasion as an evolutionary trait has been mostly ignored in theoretical frameworks. By exploring this trade-off in a novel evolutionary model, we explored the emergence of new variants and their long term evolutionary patterns. This new model reveals that highly transmissible strains often evolve towards greater immune evasion, while less contagious strains may increase in transmissibility. By deriving a non-linear difference equation from a linear trade-off assumption, we examine long-term evolutionary patterns, criteria for convergence, and cyclical strain dynamics. Our analysis also uncovers conditions

that lead to chaotic evolution, illustrated through bifurcation diagrams that showcase complex and unpredictable behaviors.

Overall, this thesis provides valuable insights into the mechanisms driving viral evolution and the effectiveness of various control measures, offering a comprehensive understanding of how pathogens evolve in response to immunity and transmission dynamics.

Publications

The dissertation is based on the following two published papers:

1. Sayyar, G., and Röst, G. (2023) Epidemic Patterns of Emerging Variants with Dynamical Social Distancing. *In: Mondaini, R.P. (eds) Trends in Biomathematics: Modeling Epidemiological, Neuronal, and Social Dynamics. BIOMAT 2022. Springer, Cham, 215–232*. https://doi.org/10.1007/978-3-031-33050-6_13

2. Sayyar, G., Garab, Á., Röst, G. (2025) Evolution into chaos – implications of the trade-off between transmissibility and immune evasion. *Infectious Disease Modelling 10(3), 909–923*. https://doi.org/10.1016/j.idm.2025.04.003.

Further publications of the author:

3. Morison, C., Fic, M., Marcou, T., Mohamadichamgavi, J., Antón, J. R., **Sayyar, G.**, Stein, A., Bastian, F., Krakovská, H., Krishnan, N., Pires, D. L. (2025) Public Goods Games in Disease Evolution and Spread. *Dynamic Games and Applications, 1–17.* https://doi.org/10.1007/s13235-025-00619-5

4. Sayyar, G., Hosseini, S. M., & Mostajeran, F. (2021). A high-order scheme for time-space fractional diffusion equations with Caputo–Riesz derivatives. *Computers & Mathematics with Applications, 104, 34–43*. https://doi.org/10.1016/j.camwa.2021.11.002

Bibliography

[1] Acevedo, M. A., Dillemuth, F. P., Flick, A. J., Faldyn, M. J., and Elderd, B. D. (2019). Virulence-driven trade-offs in disease transmission: a meta-analysis. *Evolution, 73(4), 636–647*. https://doi.org/10.1111/evo.13692

[2] Alizon, S. and van Baalen, M. (2005). Emergence of a convex trade-off between transmission and virulence. *The American Naturalist, 165(6), E155—E167*. https://doi.org/10.1086/430053

[3] Alizon, S., Hurford, A., Mideo, N., and Van Baalen, M. (2009). Virulence evolution and the trade-off hypothesis: history, current state of affairs and the future. *Journal of Evolutionary Biology, 22(2), 245–259*. https://doi.org/10.1086/285830

[4] Alizon, S., and Sofonea, M. T. (2021). SARS-CoV-2 virulence evolution: avirulence theory, immunity and trade-offs. *Journal of Evolutionary Biology, 34(12), 1867–1877*. https://doi.org/10.1111/jeb.13896

[5] AlQadi, H., Bani-Yaghoub, M. (2022). Incorporating global dynamics to improve the accuracy of disease models: Example of a COVID-19 SIR model. *Plos One, 17(4), E0265815*. https://doi.org/10.1371/journal.pone.0265815

[6] Allen, L. (2007). An introduction to mathematical biology. *Pearson*

[7] Aleem, A., Ab, A. S., and Slenker, A. K. (2021). Emerging variants of SARS-CoV-2 and novel therapeutics against coronavirus (COVID-19). *StatPearls Publishing, Treasure Island (FL), PMID: 34033342*. https://www.ncbi.nlm.nih.gov/books/NBK570580/

[8] Aquino, E. M.L., Silveira, I. H., Pescarini, J. M., Aquino, R., Souza-Filho, J., et al. (2020). Social distancing measures to control the COVID-19 pandemic: potential impacts and challenges in Brazil. *Ciencia & Saude Coletiva, 25, 2423–2446*. https://doi.org/10.1590/1413-81232020256.1.10502020

[9] Anderson, R. M., and May, R. M. (1979). Population biology of infectious diseases: Part I. *Nature*, 280(5721), 361–367.

[10] Anderson, R. M., and May, R. M. (1991). Infectious diseases of humans: dynamics and control. *Cambridge University Press*.

[11] Andersen, K. G., Rambaut, A., Lipkin, W. I., Holmes, E. C., and Garry, R. F. (2020). The proximal origin of SARS-CoV-2. *Nature Medicine, 26(4), 450–452*. https://doi.org/10.1038/s41591-020-0820-9

[12] Azizi, A., Kazanci, C., Komarova, N. L., Wodarz, D. (2022). Effect of human behavior on the evolution of viral strains during an epidemic. *Bulletin of Mathematical Biology, 84(12), 144*. https://doi.org/10.1007/s11538-022-01102-7

[13] Anshumali, M., Arun K., and Vikash V. (2022). Structural and antigenic variations in the spike protein of emerging SARS-CoV-2 variants. *PLoS Pathogens, 18(2), E1010260*. https://doi.org/10.1371/JOURNAL.PPAT.1010260

[14] Barabási, A. and Albert, R. (1999) Emergence of scaling in random networks. *Science 286(5439), 509-512*. https://doi.org/10.1126/science.286.5439.509

[15] Barabási, A. (2009) Scale-free networks: a decade and beyond. *Science 325(5939), 412-413*. https://doi.org/10.1126/science.1173299

[16] Bartha, F. A., Boldog, P., Tekeli, T., Vizi, Z., Dénes, A., and Röst, G. (2021) Potential severity, mitigation, and control of Omicron waves depending on pre-existing immunity and immune evasion. In *Trends in Biomathematics - Stability and Oscillations in Environmental, Social, and Biological Models, pages 407–419. Springer*. https://doi.org/10.1007/978-3-031-12515-7_22

[17] Barton, N. H., and Polechová, J. (2005) The limitations of adaptive dynamics as a model of evolution. *Journal of Evolutionary Biology 18(5), 1186–1190*. https://doi.org/10.1111/j.1420-9101.2005.00943.x

[18] Bauch, C.T. (2008). The Role of Mathematical Models in Explaining Recurrent Outbreaks of Infectious Childhood Diseases. *In: Brauer, F., van den Driessche, P., Wu, J. (eds) Mathematical Epidemiology. Lecture Notes in Mathematics, Springer, Berlin, Heidelberg 1945, 297–319*. https://doi.org/10.1007/978-3-540-78911-6_11

[19] Boni, M. F., Gog, J. R., Andreasen, V., and Feldman, M. W. (2006) Epidemic dynamics and antigenic evolution in a single season of influenza A. *Proceedings of the Royal Society B: Biological Sciences 273(1592), 1307–1316*. https://doi.org/10.1098/rspb.2006.3466

[20] Boots, M., and Sasaki, A. (1994) Small worlds' and the evolution of virulence: infection occurs locally and at a distance. *Proceedings of the Royal Society of London. Series B: Biological Sciences 266(1432) 1933–1938*. https://doi.org/10.1098/rspb.1999.0869

[21] Cai, Y., Zhang, J., Xiao, T., Lavine, C. L., Rawson, S., Peng, H., Zhu, H., Anand, K., Tong, P., Gautam, A., et al. (2021) Structural basis for enhanced infectivity

and immune evasion of SARS-CoV-2 variants. *Science 373(6555), 642–648*. https://www.science.org/doi/10.1126/science.abi9745

[22] Carabelli, A. M., Peacock, T. P., Thorne, L. G., Harvey, W. T., Hughes, J., de Silva Thushan I. 6, C.-. G. U. C., Peacock, S. J., Barclay, W. S., de Silva, T. I., Towers, G. J., et al. (2023). SARS-CoV-2 variant biology: immune escape, transmission and fitness. *Nature Reviews Microbiology*, 21(3), 162–177. https://doi.org/10.1038/s41579-022-00841-7

[23] Cascella, M., Rajnik, M., Aleem, A., Dulebohn, S. C., and Napoli, R. Di. (2022) Features, evaluation, and treatment of coronavirus (COVID-19). *StatPearls Publishing, Treasure Island (FL), PMID: 32150360*.

[24] Cohen, J. and Kupferschmidt, K. (2020) Countries test tactics in 'war' against COVID-19. *Science 367(6484)*. https://doi.org/10.1126/science.367.6484.128

[25] Cooper, I.,Mondal, A., and Antonopoulos, C. G. (2020) A SIR model assumption for the spread of COVID-19 in different communities. *Chaos, Solitons & Fractals 139, 110057*. https://doi.org/10.1016/j.chaos.2020.110057

[26] Cuevas, E. (2020) An agent-based model to evaluate the COVID-19 transmission risks in facilities. *Computers in Biology and Medicine 121, 103827*. https://doi.org/10.1016/j.compbiomed.2020.103827

[27] Cull, P. (2007) Population models: Stability in one dimension. *Bulletin of Mathematical Biology 69(3), 989–1017*. https://doi.org/10.1007/s11538-006-9129-1

[28] Cull, P., Walsh, K., and Wherry, J. (2008) Stability and instability in one dimensional population models. *Scientiae Mathematicae Japonicae 67(2), 105–124*. https://doi.org/10.1007/s11538-006-9129-1

[29] Dieter, E., and James, J. B. (2003) Challenging the trade-off model for the evolution of virulence: Is virulence management feasible? *Trends in Microbiology 11(1), 15–20*. https://doi.org/10.1016/S0966-842X(02)00003-3

[30] Dömling, A., and Gao, L. (2020) Chemistry and Biology of SARS-CoV-2. *Chem 6(6), 1283–1295*. https://doi.org/10.1016/j.chempr.2020.04.023

[31] Duong, D. (2021) Alpha, Beta, Delta, Gamma: What's important to know about SARS-CoV-2 variants of concern?. *CMAJ 193 (27) E1059-E1060*. https://doi.org/10.1503/cmaj.1095949

[32] Fan, Y., Li, X., Zhang, L., Wan, S., Zhang, L., and Zhou, F. (2022) SARS-CoV-2 Omicron variant: recent progress and future perspectives. *Signal Transduction and Targeted Therapy 7(1), 1–11*. https://doi.org/10.1038/s41392-022-00997-x

[33] Ferguson, N. M., Galvani, A. P., Bush, R. M. (2003) Ecological and immunological determinants of influenza evolution. *Nature 422(6930), 428-433*. https://doi.org/10.1038/nature01509

[34] Frank, SA and Schmid-Hempel, P. (2008) Mechanisms of pathogenesis and the evolution of parasite virulence. em Journal of Evolutionary Biology 21(2), 396–404. https://doi.org/10.1111/j.1420-9101.2007.01480.x

[35] Giesecke, J. (2017) Modern infectious disease epidemiology. *CRC Press*. https://doi.org/10.1201/9781315222714

[36] Gupta, S., Simon, K. I., Wing, C. (2020) Mandated and voluntary social distancing during the COVID-19 epidemic: A review. *National Bureau of Economic Research*. https://doi.org/10.3386/w28139

[37] Haraguchi, Y., and Sasaki, A. (2000) The evolution of parasite virulence and transmission rate in a spatially structured population. *Journal of Theoretical Biology 203(2), 85–96*. https://doi.org/10.1006/jtbi.1999.1065

[38] Hellewell, J., Abbott, S., Gimma, A., Bosse, N., I., and Jarvis, C. I., Russell, T. W., Munday, J. D., Kucharski, A. J., Edmunds, W. J., Sun, F., et al. (2020) Feasibility of controlling COVID-19 outbreaks by isolation of cases and contacts. *The Lancet Global Health 8(4), E488–E496*. https://doi.org/10.1016/S2214-109X(20)30074-7

[39] Hirsch, M. W., Stephen S., and Robert L. D. (2013). Differential equations, dynamical systems, and an introduction to chaos. *Elsevier Science*.

[40] Kaiming, T., Tzou, P. L., Nouhin, J., Gupta, R. K., Oliveira, T., Kosakovsky Pond, S. L., Fera, D., and Shafer, R. W. (2021) The biological and clinical significance of emerging SARS-CoV-2 variants. *Nature Reviews Genetics 22(12), 757–773*. https://doi.org/10.1038/s41576-021-00408-x

[41] Keeling, M. J., and Rohani, P. (2011) Modeling infectious diseases in humans and animals. *Princeton University Press*

[42] Kermack, W. O., and McKendrick, A. G. (1927). A contribution to the mathematical theory of epidemics. *The Royal Society, 115(772), 700–721*. https://doi.org/10.1098/rspa.1927.0118

[43] Komarova, N. L., Azizi, A., Wodarz, D. (2021) Network models and the interpretation of prolonged infection plateaus in the COVID19 pandemic. *Epidemics 35, 100463*. https://doi.org/10.1016/j.epidem.2021.100463

[44] Kun, Á., Hubai, A. G., Král, A., Mokos, J., Mikulecz, B. Á., and Radványi, Á. (2023) Do pathogens always evolve to be less virulent? The virulence–transmission trade-off in light of the covid-19 pandemic. *Biologia Futura, 74, 69–80*. https://doi.org/10.1007/s42977-023-00159-2

[45] Kuzmina, A.,Wattad, S., Khalaila , Y., Engel, S., Rosenberg, E., and Taube, R. (2021) SARS CoV-2 Delta variant exhibits enhanced infectivity and a minor decrease in neutralization sensitivity to convalescent or post-vaccination sera. *Iscience 24(12), 103467*. https://doi.org/10.1016/j.isci.2021.103467

[46] Li, T. Y. and Yorke, J. A. (1975) Period three implies chaos. *The American Mathematical Monthly, 82(10), 985–992.*. https://doi.org/10.2307/2318254

[47] Lin, C. J., Deger, K. A., Tien, J. H. (2016) Modeling the trade-off between transmissibility and contact in infectious disease dynamics. *Mathematical Biosciences 277, 15–24*. https://doi.org/10.1016/J.MBS.2016.03.010

[48] Lobinska, G., Pauzner, A., Traulsen, A., Pilpel, Y., and Nowak, M. A. (2022) Evolution of resistance to COVID-19 vaccination with dynamic social distancing. *Nature Human Behaviour 6(2), 193–206*. https://doi.org/10.1038/s41562-021-01281-8

[49] Lyngse, F. P., Kirkeby, C. T., Denwood, M., et al.(2022) Household transmission of SARS-CoV-2 Omicron variant of concern subvariants BA. 1 and BA. 2 in Denmark. *Nat Commun 13, 5760*. https://doi.org/10.1038/s41467-022-33498-0

[50] Maheshwari, P., and Albert, R. (2020). Network model and analysis of the spread of Covid-19 with social distancing. *Applied Network Science*, 5(1), 100. https://doi.org/10.1007/s41109-020-00344-5

[51] Martcheva, M. (2015) An introduction to mathematical epidemiology. *Springer New York, NY*. https://doi.org/10.1007/978-1-4899-7612-3

[52] Masuda, N., and Vestergaard, C. L. (2022) Gillespie algorithms for stochastic multiagent dynamics in populations and networks. *Cambridge University Press*. https://doi.org/10.1017/9781009239158

[53] Mattioli, A. V., Ballerini Puviani, M., Nasi, M., and Farinetti, A. (2020) COVID-19 pandemic: the effects of quarantine on cardiovascular risk. *European Journal of Clinical Nutrition 74(6), 852–855*. https://doi.org/10.1038/s41430-020-0646-z

[54] Memon, Z., Qureshi, S., and Memon, B. R. (2021) Assessing the role of quarantine and isolation as control strategies for COVID-19 outbreak: a case study. *Chaos, Solitons & Fractals 144, 110655*. https://doi.org/10.1016/j.chaos.2021.110655

[55] Mengist, H. M.,Kombe, A. J. k., Mekonnen, D., Abebaw, A., Getachew, M., and Jin, T. (2021) Mutations of SARS-CoV-2 spike protein: Implications on immune evasion and vaccine-induced immunity. *Seminars in Immunology 55. Academic Press* https://doi.org/10.1016/J.SMIM.2021.101533

[56] Messenger, S. L., Molineux, I. J., and Bull, J. J. (1999) Virulence evolution in a virus obeys a trade off. *The Royal Society, 266(1417), 397–404*. https://doi.org/10.1098/rspb.1999.0651

[57] Messenger, S. L., Molineux, I. J., and Bull, J. J. (1994) Virulence evolution in a virus obeys a trade off. *The Royal Society, 266(1417), 397–404*. https://doi.org/10.1098/rspb.1999.0651

[58] Mitchell, C., and Kribs, C. (2019) Invasion reproductive numbers for periodic epidemic models. *Infectious Disease Modelling 4, 124–141*. https://doi.org/10.1016/J.IDM.2019.04.002

[59] Mohsin, M., and Mahmud, S. (2022) Omicron SARS-CoV-2 variant of concern: A review on its transmissibility, immune evasion, reinfection, and severity. *Medicine 101(19), E29165*. https://doi.org/10.1097/MD.0000000000029165

[60] Msemburi, W., Karlinsky, A., Knutson, V., Aleshin-Guendel, S., Chatterji, S., and Wakefield, J. (2023) The WHO estimates of excess mortality associated with the COVID-19 pandemic. *Nature 613(7942), 130–137*. https://doi.org/10.1038/s41586-022-05522-2

[61] Nande, A., Adlam, B., Sheen, J., Levy, M. Z., and Hill, A. L. (2021). Dynamics of COVID-19 under social distancing measures are driven by transmission network structure. *PLoS Computational Biology, 17(2), E1008684*. https://doi.org/10.1371/journal.pcbi.1008684

[62] Nguyen, N. h. L., Kim, S., Lindemann, G., and Berry, V. (2021) COVID-19 Spike Protein Induced Phononic Modification in Antibody-Coupled Graphene for Viral Detection Application. *ACS Nano 15(7), 11743–11752*. https://orcid.org/0000-0002-1102-1996

[63] Nørgaard, L. S., Zilio, G., Saade, C., Gougat-Barbera, C., Hall, M.D., Fronhofer, E. A., and Kaltz, O. (2021) An "evolutionary trade-off between parasite virulence and dispersal at experimental invasion fronts. *Ecology Letters 24(4), 739–750*. https://doi.org/10.1111/ELE.13692

[64] Nowak, M. A. (2006) Evolutionary dynamics. *Harvard University Press, U.S.A*. https://doi.org/10.2307/j.ctvjghw98

[65] Otto, S. P., MacPherson, A. and Colijn, C. (2024) Endemic does not mean constant as SARS-CoV-2 continues to evolve. *Evolution 78(6), 1092–1108.*, https://doi.org/10.1093/evolut/qpae041

[66] Péni, T., Csutak, B., Szederkényi, G., and Röst, G. (2020). Nonlinear model predictive control with logic constraints for COVID-19 management. *Nonlinear Dynamics, 102, 1965–1986*. https://doi.org/10.1007/s11071-020-05980-1

[67] Rajnarayanan, R. (2023) Immune Escape vs ACE2 Binding (relative to BA2)–20DayTrends–Global. https://public.tableau.com/app/profile/raj.rajnarayanan/viz/ImmuneEscapevsACE2BindingrelativetoBA2-20DayTrends-Global/Dashboard22

[68] Restif, O., and Koella, J. C. (2003) Shared control of epidemiological traits in a coevolutionary model of host-parasite interactions. *The American Naturalist 161(6), 827–836*. https://doi.org/10.1086/375171

[69] Riou, C., Keeton, R., Moyo-Gwete, T., Hermanus, T., Kgagudi, P., Baguma, R., et al. (2021) Escape from recognition of SARS-CoV-2 variant spike epitopes but overall preservation of T cell immunity. *Science Translational Medicine, 14(631), eabj6824*. https://doi.org/10.1126/scitranslmed.abj6824

[70] RIVM - Dutch National Institute for Public Health and the Environment. (2022) Variants of the coronavirus SARS-CoV-2. https://www.rivm.nl/en/coronavirus-covid-19/virus/variants

[71] Röst, G., Bartha, F. A., Bogya, N., Boldog, P., Dénes, A., Ferenci, T., et al (2020) Early phase of the COVID-19 outbreak in Hungary and post-lockdown scenarios. *Viruses*, 12(7), 708. https://doi.org/10.3390/v12070708

[72] Saad-Roy, C. M., Morris, S. E., Metcalf, C. J. E., Mina, M. J., Baker, R. E., Farrar, J., Holmes, E. C., and Colijn, C. (2021) Epidemiological and evolutionary considerations of SARS-CoV-2 vaccine dosing regimes. *Science 372(6540), 363–370*. https://doi.org/10.1126/science.abg8663

[73] Sayyar, G., and Röst, G. (2023) Epidemic Patterns of Emerging Variants with Dynamical Social Distancing. *In: Mondaini, R.P. (eds) Trends in Biomathematics: Modeling Epidemiological, Neuronal, and Social Dynamics. BIOMAT 2022. Springer, Cham, 215–232*. https://doi.org/10.1007/978-3-031-33050-6_13

[74] Schmid-Hempel, P. (2008) Parasite immune evasion: a momentous molecular war. *Trends in Ecology & Evolution 23(6), 318–326*. https://doi.org/10.1016/j.tree.2008.02.011

[75] Sedaghat, H. (2013) Nonlinear difference equations: Theory with applications to social science models. *Springer Science & Business Media 15*. https://doi.org/10.1086/430053

[76] Silva, P. C. L., Batista, P. V. C., Lima, H. S., Alves, M. A., Guimarães, F. G., and Silva, R. C. P. (2020) COVID-ABS: An agent-based model of COVID-19 epidemic to simulate health and economic effects of social distancing interventions. *Chaos, Solitons & Fractals 139, 110088*. https://doi.org/10.1016/j.chaos.2020.110088

[77] Thieme, H. R. (2018) Mathematics in population biology. *Princeton University Press*. https://doi.org/10.2307/j.ctv301f9v

[78] Tian, D., Sun, Y., Zhou, Ji., and Ye, Q. (2022) The global epidemic of SARS-CoV-2 variants and their mutational immune escape. *Journal of Medical Virology 94(3), 847–857*. https://doi.org/10.1002/jmv.27376

[79] Van Baalen, M., and Sabelis, M. W. (1994) The Dynamics of Multiple Infection and the Evolution of Virulence. *The American Naturalist 146(6), 881–910*. https://doi.org/10.1086/285830

[80] Van den Driessche, P. (2017) Reproduction numbers of infectious disease models. *Infectious Disease Modelling 2(3), 288–303*. https://doi.org/10.1016/j.idm.2017.06.002

[81] Vynnycky, E, and White, R. (2010) An introduction to infectious disease modelling. *Oxford University Press*

[82] Wang, Q., Iketani, S., Li, Z., Liu, L., Guo, Y., Huang, Y., Bowen, A. D., Liu, M., Wang, M., Yu, J., et al. (2023) Alarming antibody evasion properties of rising SARS-CoV-2 BQ and XBB subvariants. *Cell 186(2), 279–286*. https://doi.org/10.1016/j.cell.2022.12.018

[83] WHO (2024) COVID-19 Update; Total Death & Case. https://data.who.int/dashboards/covid19/deaths?n=o

[84] Woolhouse, M. E. J, and Gowtage-Sequeria, S. (2005) Host range and emerging and reemerging pathogens. *Emerging Infectious Diseases, 11(12), 1842*. https://doi.org/10.3201/eid1112.050997

[85] Yang, H. M., Lombardi Junior, L. P., and Campos, A. C. (2021) Evaluating the trade-off between transmissibility and virulence of SARS-CoV-2 by mathematical modeling. *MedRxiv, 2021-02*. https://doi.org/10.1101/2021.02.27.21252592

[86] Yang, S., Yu, Y., Xu, Y., Jian, F., Song, W., Yisimayi, A., Wang, P., Wang, J., Liu, J., Yu, L., et al. (2024) Fast evolution of SARS-CoV-2 BA. 2.86 to JN. 1 under heavy immune pressure. *The Lancet Infectious Diseases 24(2), E70–E72*. https://doi.org/10.1016/S1473-3099(23)00744-2